Comparison of Structural and Catalytic Properties of Monometallic Mo and V Oxides and M1 Phase Mixed Oxides for Oxidative Dehydrogenation

Leelavathi Annamalai,¹ Sopuruchukwu Ezenwa,¹ Yanliu Dang,² Haiyan Tan,² Steven L Suib,²,³* and Prashant Deshlahra¹*

¹Department of Chemical and Biological Engineering, Tufts University, Medford, Massachusetts 02155, USA

² Institute of Materials Science, University of Connecticut, Storrs, Connecticut 06269, USA

³ Department of Chemistry, University of Connecticut, Storrs, Connecticut 06269, USA

^{*}Corresponding authors:

Abstract

Mo and V containing oxides are among the most important oxidative dehydrogenation catalysts. The effects of differences in structure and compostion among SiO₂ supported VO_x, unsupported V₂O₅ and MoO₃ and M1 phase MoV mixed oxide catalysts on catalytic proerties are probed using their reactivity and dehydrogenation selectivity in oxidative conversion of ethane (C₂H₆) and cyclohexane (C₆H₁₂). The C₂H₆ and C₆H₁₂ activation rates are nearly insensitive to VO_x loading on SiO₂ at low loadings but decrease at high loadings due to the formation of V₂O₅ nanoparticles with low V dispersion. The C-H activation enthalpies are lower at high loadings and in unsupported V₂O₅ suggesting higher intrinsic reactivity of V₂O₅ nanoparticles. The C₂H₆/C₆H₁₂ rate ratios are below 0.01 on all VO_x/SiO₂ catalysts, consistent with weaker C-H bonds in C₆H₁₂, but are higher on V₂O₅ nanoparticles than on low loading VO_x/SiO₂ samples. MoO₃ samples exhibit lower rates and higher activation energies than VO_x/SiO₂ and V₂O₅ samples, and similar C₂H₆/C₆H₁₂ rate ratios as V₂O₅. M1 phase MoVTeNb and MoV mixed oxides contain one-dimensional micropores of size similar to C₂H₆ but much smaller than C₆H₁₂; preparation methods significantly affect their elemental composition, accessible micropore volumes and surface areas. Post-synthesis of MoVTeNbO with H₂O₂ improves M1 phase purity, and C₂H₆ and C₆H₁₂ activation rates increase that are consistent with increase in their intrapore and external surface areas. The C₂H₆ and C₆H₁₂ activation rates in MoVO without Te and Nb are higher than values predicted from MoVTeNbO and their surface micropores and external surface areas, because higher V content in these samples increases their reactivity by slightly decreasing activation energies. The C₂H₆/C₆H₁₂ rate ratios in these samples are much higher than VO_x/SiO₂, V₂O₅, and MoO₃ and roughtly correlate with internal/external surface ratios consistent with C₂H₆ and C₆H₁₂ activation occurring inside and outside the pores, respectively. The M1 phase samples exhibit much higher selectivity than VO_x/SiO₂, V₂O₅, and MoO₃, but among the M1 phase samples the selectivity is slightly lower in MoVO than in MoVTeNbO. Local structure and composition on reactivity in M1 phase oxides and oxides without heptagonal micropores, but C₂H₆/C₆H₁₂ rate ratios and C₂H₄ selectivities are much higher in the M1 phase, which confirms for a broad range of oxides previously proposed roles of micropores in activating C₂H₆ selectively.

1. Introduction

The shale gas boom has boosted the availability of C1-C4 alkanes but has also contributed to increased flaring of excess natural gas. Selective energy-efficient catalytic conversions of these hydrocarbons to useful chemicals and fuels can provide significant economic benefits and alleviate environmental concerns [1]. Ethylene (C₂H₄) is one of the most important industrial chemical building blocks. Ethylene is produced via cracking of C₂H₆ or larger hydrocarbons in large-scale energy intensive endothermic processes. Significant advances have been made in C₂H₄ production through oxidative dehydrogenation (ODH) of C₂H₆, but superior economics of the C₂H₆ steam cracking process prohibit its commercial implementation [1-3]. The exothermic nature of oxidative reactions, however, can lead to more sustainable smaller scale processes for stranded hydrocarbon resources [4, 5]. These processes can also exhibit a smaller CO₂ footprint and lower carbon usage by avoiding natural gas combustion required to provide energy in endothermic counterparts [1, 2].

Performance goals suggested for C_2H_6 ODH to be commercially viable include C_2H_4 95% selectivity at C_2H_6 conversions greater than 60% and long-term catalyst stability [1, 2]. In spite of many studies on ethane ODH catalysts and processes the desired criteria for commercialization are yet to be fully satisfied. Among the most promising catalysts is the orthorhombic M1 phase mixed oxides of Mo, V, Nb, and Te (or Sb), which exhibit the highest C_2H_4 selectivities at moderate reaction temperatures of 573-773 K [1, 2, 6-10]. Process economic estimates for such catalysts have demonstrated potential profitability [11]. Recent synthesis efforts have succeeded in preparing the orthorhombic M1 phase mixed metal oxides consisting of Mo and V without Te and Nb, which exhibited similar C_2H_4 selectivity as those with the additives [12]. The structure of these oxide is well-studied and consists of layers of linked octahedral units of MO₆ (M = Mo, V) that form five, six, and seven membered rings in the (001) crystal planes that form one-dimensional pores [12-18].

Although C₂H₆ ODH on M1 phase oxides has been widely studied, the origin of high selectivity is not well understood, and multiple reasons have been proposed. These proposals tend to invoke heuristic concepts of site-isolation, correlation of reactivity to specific outer surface facets or unique sites formed by Te or by its mobility in the lattice, without connecting selectivity to molecular conversion steps that make the unselective products and its dependence on quantitative catalyst descriptors [16, 19, 20]. These proposals overlook potential effects of the

micropores in the M1 phase on reactivity and selectivity, presumably because of the high bulk density of the transition metal oxides and partial pore blockage that lead to pore volumes much smaller than typical porous catalysts such as zeolites; however, some studies on M1 phase MoV oxides demonstrated that ethane indeed reacts inside the pores [12, 21, 22], without establishing its role in selectivity.

Recent work probed the role of such pores in C₂H₆ ODH using ethane to cyclohexane conversion rate ratios $(r_{c_2H_6}/r_{c_6H_{12}})$ and density functional theory (DFT) calculations to show that C₂H₆ activation in MoVTeNb oxides occurs predominantly inside the pores [23, 24]. The sevenmember ring pores have accessible diameter of size (0.4 nm) that provides a tight fit for C₂H₆ and provide stabilization via van der Waals (vdW) calculations but excludes C₆H₁₂; therefore, the differences in rate ratios on oxides with and without such pores provide a sensitive probe of the pore contribution to rates [23, 24]. Measured activation enthalpies as well as DFT calculations for C-H bond reactions required for C₂H₄ formation and undesired C-O bond formation reactions show that the undesired steps are suppressed in the M1 phase catalysts. DFT derived H-atom addition energies to O-atoms of oxide catalysts, strengths of vdW interactions between molecules and catalysts and the steric forces reflected in catalyst distortion required to form C-H activation and C-O bond formation transition states were determined to be relevant descriptors of reactivity and selectivity. Analysis of these descriptors on MoVTeNb and V₂O₅ oxides and in pores of MoVTeNbO showed that (i) isolation of V-sites in the M1 phase as opposed to contiguous V-sites in V₂O₅ has a small effect on C₂H₄ selectivity, and (ii) pores of MoVTeNb oxides exhibit much higher selectivty than (001) surfaces of both oxides due to vdW stablization of C-H activation transition states in the pores, steric hindrance to C-O bond formation steps at bridging O-atoms of all oxides, and the absence of accessible unselective terminal O-atoms inside the pores [24].

These recent studies utilized mixed oxide samples that lacked high phase purity, although the pore contributions originated solely from the M1 phase [23, 24], and high loading VO_x/SiO_2 samples with high abundance of V_2O_5 nanoparticles relative to isolated VO_x domains. The assessments were based on the assumption that all exposed lattice O-atoms must exhibit low C_2H_6/C_6H_{12} rate ratios due to weaker C-H bonds in C_6H_{12} , but did not provide explicit confirmaton to this assumption. Yet, V and Mo based oxides vary significantly in structure (Scheme 1), reactivity and selectivity for ODH reactions [25]. Moreover, preparation methods have significant

impact on shapes, sizes, composition, and phase purity in M1 phase crystallites as well as their reactivity [8, 20]. Correlations of some of these variations with the presence of different external facets based on changes in particle shapes have been studied. However, the role of micropore volumes and molecular probes that seek to distinguish pore contributions from structure and compostion effects in outer planes of oxides have not been studied.

Here, Mo and V based oxides of different structures and composition are prepared and the effects of these changes on catalytic properties are assessed using rates and selectivity for C_2H_6 - O_2 and C_6H_{12} - O_2 reactions. VO_x/SiO_2 samples of different V surface density, unsupported V_2O_5 and MoO3 and mixed oxides consisting of nearly pure M1 phase MoV, and MoVTeNb catalysts are prepared. The MoVTeNb oxide is modified via post-synthesis treatment with H_2O_2 . The effects of these treatments on micropore volumes, external areas, rates, selectivity, $r_{c_2H_6}/r_{c_6H_{12}}$ values, and activation energies are measured. The results show significant effects of structure and composition among the different catalysts within the family of M1 phase oxides and the family of oxides without the heptagonal pores, and yet highlight a sharp contrast between the two families that point to most C_2H_6 activations occurring within the pores of the M1 phase and to its coincidence with high C_2H_4 selectivity. These differences among catalysts within each family and between the two families are used to describe the distinct effects of abstractor strength and the local structure of the oxides.

2. Materials and methods

2.1 Catalysts synthesis

Procedures described in the literature were used to prepare M1 phase MoVTeNb oxides (MoVTeNbO) [26], post-synthesis treatment of this oxide with H₂O₂ [27], M1 phase MoV oxides (MoVO) [28], vanadium oxides supported on SiO₂ supports (VO_x/SiO₂) [29], and unsupported vanadium and molybdenum oxides (V₂O₅, MoO₃) [30]. All metal precursors were obtained from Sigma-Aldrich and used without any additional purification.

2.1.1 Synthesis of bulk MoVTeNb oxide

Ammonium molybdate tetrahydrate (9.1 g, 81-83% MoO₃ basis) was dissolved in deionized water (100 cm³) and heated to 353 K. Vanadyl sulfate (3.3g, 97%) and telluric acid (2.7g, 99%) were

added to this solution while stirring at 353K. After continuous stirring for 0.25 h, the solution was cooled down to 298K prior to the addition of a separate solution of ammonium niobate oxalate hydrate (3 g, 99.99%) in deionized water (50 cm³) at 298K. The combined solution contained 1:0.25:0.23:0.12 Mo:V:Te:Nb molar ratios. The solution was stirred for 0.5 h and transferred to a 200 cm³ Teflon vessel. Nitrogen (Airgas, 99.99%) was bubbled into the solution for 0.08 h (50 cm³ min⁻¹) to displace dissolved oxygen. The Teflon vessel was sealed in a stainless-steel autoclave and heated at 403K for 96 h in a preheated muffle furnace. The solid products obtained from this treatment were stirred with 100 cm³ deionized water for 0.17 h, recovered by vacuum filtration and dried overnight in an oven at 373K. The dried solids were crushed using mortar and pestle and treated in flowing He (50 cm³ min⁻¹ Airgas, 99.999%) in a tube furnace ramped to 873K at 0.083 K s⁻¹ and held for 2 h. This procedure [26] is expected to yield greater phase purity of M1 phase of MoVTeNbO with higher Te content than that used in our previous study [23].

2.1.2 Post-synthesis H₂O₂ treatment of MoVTeNbO

MoVTeNbO samples prepared using a procedure described above have been reported to contain minority M2 phase impurities and these samples were treated in hydrogen peroxide to improve the purity of the desired M1 phase [27, 31, 32]. The MoVTeNbO sample was crushed and sieved to retain particles smaller than 106 μ m. Four g of this sample was stirred in 100 cm³ 10% aqueous hydrogen peroxide solution (Sigma Aldrich) at 333K for 3 h, collected by centrifugation and dried overnight at 373K in an oven.

2.1.3 Synthesis of MoVO samples

Ammonium molybdate tetrahydrate (8.8 g, 81-83% MoO₃ basis) was dissolved in deionized water (120 cm³) and added to an aqueous solution of vanadyl sulfate (3.3 g in 120 cm³) at 298K. The combined solution contained 1:0.25 Mo:V molar ratios. This solution was stirred for 0.17 h and transferred to two Teflon vessels. A 100 cm³ vessel contained 75 cm³ solution while a 200 cm³ vessel contained 165 cm³ solution. Nitrogen was bubbled through both vessels (40 cm³ min⁻¹) for 0.08 h to remove dissolved oxygen, which were then sealed in stainless-steel autoclaves and treated at 448K for 48 h in a preheated muffle furnace. The solids deposited inside the walls of Telfon vessels were separated using a plastic spatula, stirred in 1000 cm³ deionized H₂O for 0.5 h,

recovered by vacuum filtration, and dried overnight in an oven at 373K. The dried solid was treated with oxalic acid solution. This latter step has been reported to eliminate amorphous phases in the final product [28]. Oxalic acid (3.2 g; Sigma Aldrich, > 99%) was dissolved in 80 cm³ of deionized water and heated to 333K prior to the addition of dried solids (3.5 g). The contents were stirred for 0.5 h at 333K and washed with 1000 cm³ deionized water. The solids were recovered by vacuum filtration and dried overnight at 373K in an oven, ground using mortar and pestle, and in flowing He (50 cm³ min⁻¹, 99.999% Airgas) in a tube furnace ramped to 673K at 0.167 K s⁻¹ and held for 2 h.

2.1.4 Synthesis of VOx/SiO2 and V2O5 samples

Vanadium oxide was supported on silica at different weight loadings (VO_x/SiO₂, 1.5, 6.5 and 11.5 % V₂O₅ wt.) using incipient wetness impregnation [29, 33]. To prepare the 1.5 wt. % sample a solid mixture of ammonium metavanadate (45 mg; 99%) and oxalic acid (71 mg; \geq 99%) was dissolved in deionized water (2.3 cm³) to form a clear homogeneous deep blue solution, which was added dropwise to silica (2 g; Sigma-Aldrich Davisil Grade 633, \geq 99%, 480 m² g⁻¹, 0.75 cm³ g⁻¹; washed using 0.5 M nitric acid) and mixed using a spatula. The resulting incipiently wet solid was held at 298K for 1 h and dried overnight at 373K in an oven. The dried solids were treated in flowing air in a tube furnace ramped to 773K at 0.167 K s⁻¹ and held for 8 h. The samples with 6.5 and 11% wt. V₂O₅ were prepared using an identical procedure using proportionately greater amounts of both ammonium metavanadate and oxalic acid (Table 2).

 VO_x/SiO_2 samples with 41% wt. V_2O_5 were prepared using a wet impregnation [23]. Oxalic acid (2.94 g; \geq 99%) was dissolved in 196 cm³ of deionized water. Ammonium metavanadate (1.96 g; 99%) was added under continuous stirring at 298 K to yield 1:1.5:100 molar ratios for oxalic acid:V:H₂O. Silica powder (2.5 g; Davisil grade 633, \geq 99%, 480 m² g⁻¹; washed in 0.5 M nitric acid) was added to the solution, and stirred for 0.5 h at 373 K. The resulting slurry was dried overnight at 373K in an oven. The solid was treated in flowing air (50 cm³ min⁻¹) in a tube furnace ramped to 873K at 0.083 K s⁻¹ and held for 6 h. Unsupported V₂O₅ was prepared by treating ammonium metavanadate in flowing air (50 cm³ min⁻¹) in a tube furnace heated to 773K at 0.083 K s⁻¹ and held for 3 h [30].

2.1.5 Synthesis of MoO3 samples

Treatment of ammonium molybdate tetrahydrate loaded in a quartz boat in a tubular furnace at 773K (0.083 K s⁻¹) for 3 h under constant air flow (50 cm³ min⁻¹) yielded unsupported MoO₃.

2.2 Catalysts characterization

Powder X-ray diffraction (XRD) patterns of catalyst samples were collected using a Rigaku Ultima IV diffractometer with a monochromatic Cu K α radiation generated by a 44 mA electron beam accelerated at 40 kV. The diffraction patterns were collected at a scan rate of 0.0167° s⁻¹ with a step size of 0.01°. Bulk elemental compositions of the catalysts were determined using inductively coupled plasma atomic emission spectroscopy (ICP-AES, Leeman laboratories PS-1000). The morphology of the catalysts was inspected using an FEI Nova NanoSEM 450 scanning electron microscope (SEM) equipped with a Schottky emitter and a through-lens detector, and operated at an acceleration voltage of 5 kV with a 2 μ m beam spot size. The HAADF-STEM images were acquired on a probe-corrected Titan Themis microscope operating at 300 kV. Micropore volumes of the MoV based oxide catalysts were determined from volumetric N₂ and CO₂ physisorption isotherms obtained at 77 and 298K respectively, on a Quantachrome Autosorb iQ2 apparatus. The N₂ and CO₂ physisorption measurements were performed on 0.2 g and 0.1 g, respectively, of manually ground and pelletized (106-180 μ m) catalyst samples. The samples were degassed at 573K in flowing He for 3 h prior to the uptake measurements.

2.3 Measurements of rates and product selectivities

Catalyst samples were finely ground (<106 µm), pressed, crushed and sieved, with or without dilution with SiO₂, to retain 106-180 µm aggregates. These aggregates were held as vertical fixed beds in a U-tube quartz reactor. The reactor contains a quartz frit to hold the catalyst samples and temperature of the catalyst bed was measured using a K-type thermocouple (Omega) placed within a dimple at the reactor wall and temperatures were set using a resistive furnace (National Element) and an electronic controller (Watlow, EZ-ZONE). Prior to introduction of the reactants, the catalysts were preheated to reaction temperatures in flowing He (Airgas, 99.999%). Gaseous reactants (25% C₂H₆/He and 25% O₂/He) and diluent He were metered electronically using mass flow controllers (Porter Instruments), while the liquid reactant C₆H₁₂ (99.9%, Sigma-Aldrich) was

vaporized into the O₂/He streams using a liquid syringe pump (Cole Parmer). Temperatures of process transfer lines were maintained above 363K to prevent condensation of reactants and products. The reactor effluents were analyzed by a gas chromatograph (Agilent 7890B) equipped with a capillary column HP-PLOT Q or HP-1MS connected to a flame ionization detector, and a Carboxen-1000 packed column connected to a thermal conductivity detector. Conversions and selectivity are reported on a carbon mole basis.

Rates and product selectivity were measured at alkane conversions below 10% to prevent significant effects of reactant depletion on measured rates. Rates are normalized by total number of V atoms in MoVTeNbO, MoVO, VO_x/SiO₂ and by total number of Mo atoms in MoO₃. Gas phase C-H activations were ruled out through blank reactor measurements carried out at highest temperatures at conditions representative of rate measurements, which gave negligible conversions (X) for C₂H₆ (X < 0.01% at 733K, 3 kPa C₂H₆, 3 kPa O₂, 30 cm³ min⁻¹) and C₆H₁₂ (X < 0.1% at 648K, 3 kPa C₂H₆, 3 kPa O₂, 30 cm³ min⁻¹). Similar measurements were carried out on silica packed reactors which showed negligible effects of support alone on the ODH reaction conversions.

The absence of external mass transfer limitations was confirmed through space velocity experiments which did not show any significant change in observed rate beyond that observed from product inhibition or reactant depletion in the assumed differential mode (Fig. S2). The results from intra-pellet dilutions and theoretical C₂H₆/C₂H₄ translation studies within micropores strongly suggest that the experimentally measured rates are devoid of transport limitations [12, 23] and that the absence of intrapellet concentration or temperature gradients lead to uniform local concentrations and temperatures in the catalyst bed as those of the surrounding fluid phase. Thus, the measured rates reported in this work reflect the intrinsic chemical reaction rates.

3. Results and discussion

3.1 Composition and physical properties of monometallic oxides and M1 phase mixed oxides

VO_x/SiO₂ samples with 1.5%, 6.5%, 11%, and 41% V₂O₅ wt. loading, unsupported V₂O₅ and MoO₃ samples, and M1 phase MoVTeNb, and MoV mixed oxides were prepared. Figure 1 shows XRD patterns of the monometallic and the mixed oxides. Figures 2 and 3 show SEM images of M1 phase crystals and atomic scale HAADF-STEM images of the pore structure characteristic of

these samples, respectively. Figure 4 shows N₂ and CO₂ physisorption measurements for M1 phase oxides and unsupported monometallic oxides. The compositions and surface areas of monometallic and mixed oxides are shown in Tables 1-3.

3.1.1 Crystallinity, morphology and elemental composition

The 1.5 wt% VO_x/SiO₂ sample does not show detectable XRD peaks because such low loadings form monomeric tetrahedral VO_x species on the amorphous SiO₂ domains without significant amounts of V₂O₅ nanoparticles (Fig. 1a) [34]. The 1.5%, 6.5%, and 11% VO_x/SiO₂ samples have theoretical surface densities 0.2, 1, and 1.7 V nm⁻², respectively (Table 1), based on the surface area of untreated bare SiO₂ (480 m² g⁻¹), which are well below theoretical monolayer density near 3 V nm⁻². In contrast, 41% VO_x/SiO₂ samples with a surface density of 9.6 V nm⁻² lead to XRD patterns nearly identical to unsupported V₂O₅, suggesting high abundance of V₂O₅ nanoparticles at high loadings. Raman studies have shown that some nanoparticles appear at loadings 1.8 V nm⁻ ² in catalysts prepared using ammonium metavanadate precursors and are more abundant at high loadings [34, 35]. Thus, we expect predominantly monovanadates with tetrahedral V-oxo species connected to Si in 1.5-11% VO_x/SiO₂ and predominantly bulk orthorhombic phase with contiguous octahedral V-oxo groups in 41% VO_x/SiO₂ (Scheme 1). The XRD patterns of the unsupported V₂O₅ and MoO₃ groups were consistent with their known orthorhombic phases that do not contain micropores (Fig. 1a,b) [36, 37]. Samples with low MoO_x surface density are not analyzed here because they gave undetectable C₂H₆ conversions at low reaction temperature of 648K used for other samples in Section 3.2 due to the less reactive nature of isolated MoO_x domains than the VO_x counterparts.

The XRD patterns of MoVTeNbO, H_2O_2 treated MoVTeNbO and MoVO samples are similar (Fig. 1c) and are consistent with the Miller indices for the M1 phase reported in the Inorganic Crystal Structure Database (ICSD) exhibiting major diffraction lines at $2\theta = 6.6$, 7.7, 8.9, 22.1, 27.1 and 45° (ICSD 55097 [16]. These mixed oxides must, therefore, contain the pentagonal, hexagonal, and heptagonal micropores that are part of the M1 phase crystal structure. However, the MoVTeNbO sample displayed additional peaks at $2\theta = 28.1$, and 36.1° , suggesting that this sample contains small amounts of the M2 phase (ICSD 55098 [38]) with only hexagonal pores that are much smaller than C_2H_6 molecules [39, 40]. This minority M2 phase tends to contain

Nb/Mo and Te/Mo ratios lower and higher, respectively, than the M1 phase [16, 41]. No other phases such as M₅O₁₄ were observed, which shows that the synthesized mixed oxides exhibit high M1 phase purity [23, 42]. The diffraction peaks of the undesired M2 phase in MoVTeNbO diminish markedly upon H₂O₂ treatment. These results are in good agreement with the previous reports proposing that the H₂O₂ treatment selectively dissolves the M2 phase from the structure (Fig. 1c) [27, 32, 43].

The bulk atomic composition of the MoVTeNbO before and after H₂O₂ treatment correspond to the Mo₁V_{0.23}Te_{0.25}Nb_{0.17} and Mo₁V_{0.24}Te_{0.12}Nb_{0.23} stoichiometries, respectively (Table 2). The Nb/Mo ratio increased while the Te/Mo ratio decreased significantly upon H₂O₂ treatment and the V/Mo ratio remained nearly unchanged, consistent with the removal of a Te-rich and Nb deficient M2 phase (Fig. 1c). The V/Mo ratio in the MoVO sample is 0.52, which suggests a higher V concentration than MoVTeNbO, potentially because V sites occupy pentagonal and hexagonal channels that are preferentially occupied by Nb and Te in the oxide with four cations.

The SEM images of MoVTeNbO show aggregates of plate like structures with sharp edges and corner and flat facets that are partially aggregated and interconnected (Fig. 2a,b). These samples also contain small amounts of the M2 phase (Fig. 1c) and can involve intergrown M1 and M2 phases, which has been shown to occur in these mixed oxides [32, 39, 41]. Such intergrowth may block accessibility to some pores and surfaces of the M1 phase. The samples treated with H2O2 exhibit particles of similar size and shape as the untreated MoVTeNbO samples but appear less interconnected and have less sharp corners and edges (Fig. 2c,d). These changes in morphology and the concomitant removal of the M2 phase evident in XRD patterns suggest that the H2O2 treatment may lead to more accessible surfaces and pores in the M1 phase. The MoVO samples without Nb and Te exhibit much longer rod-like structures with lengths of about 1 μm (Fig. 2e,f), which is consistent with previous observations that excluding Nb precursor favors longer rods [28, 44].

HAADF-STEM images of the (001) planes at ends of a rod from the H₂O₂ treated MoVTeNbO sample show the pentagonal, hexagonal, and heptagonal channels characteristic of M1 phase (cyan, red, and yellow polygons in Fig. 3b) [20, 45]. The intergrowth of M2 phase noticed in some literature is not observed here [39], which is consistent with the removal of the M2 phase by H₂O₂ treatment. The different framework metal atom positions in these images

display similar atomic contrasts, suggesting that preferred V atom locations in the lattice cannot be determined from visual inspection. The centers of the pentagonal rings are nearly as bright as the framework atoms suggesting nearly complete filling of these channels, potentially by Nb atoms that are known to occupy these channels. The centers of the hexagonal channels are much fainter than the framework locations, suggesting significant but partial filling of these channels. In contrast, many heptagonal channels are completely dark, but some have very faint spots, suggesting that these larger channels are often unoccupied and occasionally partially occupied. These features are typical of pure M1-phase catalyst samples [46, 47], and suggest that the heptagonal pores must be accessible for catalysis for molecules that are sufficiently small to enter these pores.

Another MoVTeNbO sample reported previously [23] was prepared and using hydrothermal treatments at 448K instead of the 403K temperature used for this work. These higher hydrothermal treatment temperature samples are denoted MoVTeNbO-ht in Tables 2 and 3. The MoVTeNbO-ht samples exhibited 1/0.27/0.02/0.09 Mo/V/Te/Nb ratios with lower Nb and Te contents than MoVTeNbO and formed significant amounts of tetragonal M_5O_{14} phase in addition to the majority M1 phase. However, the M1 phase particles in this sample were larger in size with typical lengths of plates well over 1 μ m [23].

3.1.2 Surface areas and micropore volumes

The surface areas of VO_x/SiO_2 samples derived from N_2 uptakes at pressures 0.05-0.35 of the saturation pressure (P/P₀ values) at 77K and the Brunauer-Emmett-Teller (BET) theory [48] (uptakes as a function of P/P₀ shown in Supporting Information, Fig. S3). The areas decreased significantly with increased V loading (246 and 35 m²g⁻¹ for 1.5 and 41 wt.%,; Table 1), which is consistent with the blocking of the pores in the mesoporous SiO₂ support by V₂O₅ nanoparticles at higher loadings [33], as well as with weight addition by heavier VO_x domains without significant addition to surface area. The surface areas of V₂O₅ and MoO₃ samples are much lower than VO_x/SiO₂ (8.1 and 4.5 m²g⁻¹ for V₂O₅ and MoO₃; Table 1), consistent with heavier metal ions and lower porosity in the unsupported oxides.

The N_2 uptake at 77K and CO_2 uptake at 298K as a function of pressure, expressed as a fraction of saturation pressures of these gases at the corresponding temperatures (P/P₀; P₀ = 1 and

64 atm for N₂ at 77K and CO₂ at 298K, respectively), for unsupported V₂O₅, MoO₃, and the M1 phase mixed oxides are shown in Figure 4 and in Figure S4. These uptakes are shown as gas volumes per V or Mo atom in Figure 4 and per gram of sample in Figure S4. The conversion to volumes per V or per Mo was performed by multiplying the volumes per gram to the formula weights of the catalysts based on the metal compositions as shown in Tables 1 and 2. This conversion was done in order to compare micropore volumes and areas with the reaction rates in Sections 3.2 that are also normalized by the total number of V or Mo atoms. The M1 phase samples show a steep uptake at P/P₀ values below 10⁻³ (Fig. 4a inset and Fig. 4b), which is consistent with micropore filling. Both N₂ and CO₂ uptakes in the unsupported V₂O₅ and MoO₃ samples are much lower than the M1 phase samples and the uptakes did not increase steeply at low P/P₀ values. Thus, the unsupported samples do not contain micropores small enough to allow access to C₂H₆ but restrict cyclohexane as in the case of heptagonal pores of the M1 phase.

N₂ and CO₂ uptakes at 0.002 P/P₀ values were used to estimate the volumes of small micropores in the M1 phase samples [40]. The N2 uptakes tend to give inaccurate assessments of small micropores due to slow diffusion at 77K, especially when the pores are partially blocked by cations [49]. The low thermal energy and quadrupole moment of N₂ molecules limit their access into these narrow micropores and would require unreasonably long experimental periods to ensure micropore filling [38]. The CO₂ molecules with slightly smaller kinetic diameter than N₂ and measurements at ambient temperature instead of 77K has been shown to overcome such inaccuracies [50, 51]. The N₂ uptakes are 1.1, 3.5, and 2.9 cm³g⁻¹ for MoVTeNbO, H₂O₂ treated MoVTeNbO, and MoVO samples, which correspond to respective micropore volumes of 15.5, 50.1, and 40.5×10^{-4} cm³ g⁻¹, and internal micropore areas of 15.5, 50.1 and 40.5 m² g⁻¹ or 2.5, 7.6 and 2.5×10^{-20} m² V⁻¹ (Table 3). The CO₂ uptakes are 0.8, 3.7 and 6.0 cm³g⁻¹ for MoVTeNbO, H₂O₂ treated MoVTeNbO and MoVO samples, which correspond to respective micropore volumes of 13.6, 65.7 and 105.3×10^{-4} cm³ g⁻¹, and internal micropore areas of 13.6, 65.7 and 105.3 m² g⁻¹ or 2.2, 9.9 and 6.3×10^{-20} m² V⁻¹ (Table 3). The micropore volume for the MoVo sample (105.3 × 10⁻⁴ cm³ g⁻¹) is about 45% of the theoretical volume of heptagonal pores estimated in the literature [49]. These data show that micropore volumes (and areas) from N₂ and CO₂ uptakes are similar for MoVTeNbO samples, but the latter molecule gives slightly higher values for H₂O₂ treated MoVTeNbO samples and much higher values for MoVO samples. For both probe molecules the

micropore volumes for the MoVTeNbO sample are increased more than three times upon H₂O₂ treatment, which suggests that the removal of the minority M2 phase (Fig. 1c, 2a,b) makes much greater fractions of micropores accessible to reactants potential by removing layers of oxides blocking the pores. The micropore volumes per gram of the sample are the highest for the MoVO sample, but this sample also contains a greater fraction of V atoms, and therefore, the volumes per V in this sample are lower than H₂O₂ treated MoVTeNbO.

The external surface areas derived from N₂ uptakes at 0.05-0.35 P/P₀ values and the BET equation are 9.8, 23.1 and 20.1 m² g⁻¹ or 1.6, 3.5 and 1.3 × 10⁻²⁰ m² V⁻¹ for MoVTeNbO, H₂O₂ treated MoVTeNbO and MoVO samples, respectively (Table 3). These values show that samples with higher micropore volume also exhibit larger external surface areas. The surface area for the H₂O₂ treated MoVTeNbO sample is much higher than the untreated one, suggesting that the removal of intergrowth of M₂ phases also leads to rougher surfaces and increased outer area via separation of interconnected particles, as observed in the SEM images (Fig. 2). The MoVTeNbO-ht sample with higher temperature hydrothermal treatment reported in our previous work had lower micropore volume and surface areas than all M₁ phase samples prepared in this work due to larger M₁ phase particles as well as the presence of phase impurities (Table 3).

Thus, we have prepared a series of samples with SiO₂ supported monovanadates and crystalline V₂O₅ and MoO₃ oxides without the small micropores that precisely restrict access of molecules larger than C₂H₆, and M1 phase samples with varying surface and bulk elemental compositions and accessible micropore volumes and surface areas. Next, we probe the effects of these differences in activation rates of C₂H₆ and C₆H₁₂ (cyclohexane) molecules.

3.2 C_2H_6 and C_6H_{12} activation rates and rate ratios on monometallic and mixed oxides

Activation of alkanes and cycloalkanes on metal oxides occur via Mars van Krevelen redox cycles with C-H bond activation at lattice O-atoms as the step that determines the activation rates [52]. Figure 5 shows C₂H₆ and C₆H₁₂ activation rates and C₂H₆/C₆H₁₂ rate ratios on VO_x/SiO₂ samples with different loadings and on the unsupported V₂O₅ sample. For low surface densities both C₂H₆ and C₆H₁₂ activation rates do not change significantly with VO_x loading (Fig. 5a; 1.5-11% wt. V₂O₅; 0.2-1.7 V nm⁻²), which is consistent with Raman spectroscopy studies suggesting the prevalence of predominantly monomeric tetrahedral structures at surface densities well below the

monolayer coverage limit (\sim 3 V/nm²) [35]. Surface loadings closer to a monolayer tend to form V₂O₅ crystals that are more active than VO_x monomers [35]. However, large V₂O₅ particles at loadings well above a monolayer make most V-loadings inaccessible, which leads to rates lower than VO_x monomers at 9.6 V nm⁻² when rates are normalized by all V atoms (Fig. 5a, 41 wt. % VO_x/SiO₂). The C₂H₆ and C₆H₁₂ rates on unsupported V₂O₅ are similar to 41% VO_x/SiO₂, which suggests that both samples exhibit similar V-atom accessibility (Fig. 5a). The C₂H₆/C₆H₁₂ rate ratio on all samples are over two orders of magnitude lower than unity of all VO_x/SiO₂ and V₂O₅ samples (Fig. 5b), suggesting that C₂H₆ activation energy is larger than C₆H₁₂ activation energy on all these samples. The rate ratios in the high loading samples and the V₂O₅ sample, however, are about two times that of the low loading samples (Fig. 5b, ratio \sim 0.004 for 1.5-11wt% VO_x/SiO₂, 0.008-0.01 for 41wt%VO_x/SiO₂ and V₂O₅). These lower rate ratios in monovanadates suggest that activation energy differences between C₂H₆ and C₆H₁₂ are slightly higher in monovanadates than in V₂O₅.

Figure 6 shows C_2H_6 and C_6H_{12} activation rates and C_2H_6/C_6H_{12} rate ratios on unsupported V_2O_5 , MoO_3 , and M1 phase catalysts. The BET surface area of V_2O_5 samples is nearly identical to the MoO_3 sample (Table 1; 0.12×10^{-20} m² V⁻¹ and 0.11×10^{-20} m² Mo⁻¹), indicating that the number of accessible surface sites per metal atom are not very different in these two samples. Yet, the C_2H_6 activation rate on V_2O_5 is nearly an order of magnitude higher than MoO_3 (Fig. 6a; 1.6×10^{-6} V⁻¹ s⁻¹ and 1.9×10^{-7} Mo⁻¹ s⁻¹), because the lattice O-atoms in V_2O_5 are much more reactive than MoO_3 [53]. The C_6H_{12} activation rates are also much higher on V_2O_5 than on MoO_3 (Fig. 6a), and the C_2H_6/C_6H_{12} rate ratios are very similar in the two oxides (Fig. 6b). Based on these results we expect that, for M1 phase oxides, lattice O-atoms connected to V-atoms are also more active for C-H activation than those connected solely to Mo-atoms, which is also consistent with DFT probes of reactivity based on H-atom addition energies [23, 24]. Therefore, rates on MoVTeNb and MoV mixed oxides are normalized by the number of V-atoms instead of the Mo atoms.

The C₂H₆ activation rates on MoVTeNbO, H₂O₂ treated MoVTeNbO samples are 47, 256, and 742 times the rate on V₂O₅, respectively, while the C₆H₁₂ rates are only 1, 6, and 6 times the corresponding rate on V₂O₅ (Fig. 6a). Consequently, the C₂H₆/C₆H₁₂ rate ratios on MoVTeNbO, H₂O₂ treated MoVTeNbO samples are 51, 44, and 128 times the ratio on V₂O₅. These values show that all of the M1 phase samples considered here are disproportionately much more reactive C₂H₆

than to C_6H_{12} when activation C_6H_{12} rates are used normalize the intrinsic reactivity differences for C-H activation among these oxides. As discussed in recent work [23, 24], the size of the heptagonal pores in the M1 phase (0.4nm) can allow C_2H_6 molecules to enter (0.4 nm) [21] and exclude the much larger C_6H_{12} molecules (0.6 nm) [54] (Scheme1). Thus, the C_2H_6 rate includes contributions from the internal pores and external surfaces while the C_6H_{12} rates only include contributions from external surfaces, leading to C_2H_6/C_6H_{12} activation rate ratios ($r_{C_2H_6}/r_{C_6H_{12}}$) given by:

$$\frac{r_{C_2H_6}}{r_{C_6H_{12}}} = \frac{r_{C_2H_6}^{int} + r_{C_2H_6}^{ext}}{r_{C_6H_{12}}^{ext}} = \frac{r_{C_2H_6}^{int}}{r_{C_6H_{12}}^{ext}} + \frac{r_{C_2H_6}^{ext}}{r_{C_6H_{12}}^{ext}}$$
(1)

where, $r_{C_2H_6}^{int}$ and $r_{C_2H_6}^{ext}$ represent C₂H₆ rates inside the pores and on external surfaces, and $r_{C_6H_{12}}^{ext}$ represents the C₆H₁₂ activation rate on external surfaces. The VO_x/SiO₂, unsupported V₂O₅, and the MoO₃ samples do not contain pores of precise size that allow C₂H₆ but restrict C₆H₁₂ (Scheme 1, Fig. 4). Therefore, all C₂H₆ and C₆H₁₂ molecules can access the same sites that are considered here to be external sites. The measured $r_{C_2H_6}/r_{C_6H_{12}}$ values on these samples represent $r_{C_2H_6}^{ext}/r_{C_6H_{12}}^{ext}$, which is invariably much less than unity irrespective of the structure of VO_x or MoO_x species involved (< 0.01, Fig. 5b, 6b), because of stronger C-H bonds in C₂H₆ relative to C₆H₁₂ (DFT derived C-H bond dissociation enthalpy, BDE, 422 and 408 kJ mol⁻¹, respectively) [23]. In contrast, on MoVTeNbO, H2O2 treated MoVTeNbO and MoVO, the ratio is measured to be much closer to unity (0.48, 0.42, and 1.34, respectively), which suggests that the $r_{C_2H_6}^{int}/r_{C_6H_{12}}^{ext}$ is about two orders of magnitude larger than the $r_{C_2H_6}^{ext}/r_{C_6H_{12}}^{ext}$ based on measurements of the latter ratio on several oxides without micropores. This much larger $r_{C_2H_6}^{int}/r_{C_6H_{12}}^{ext}$ value suggest that most C_2H_6 activations in M1 phase occur within micropores. The pore contributions are larger than the contributions of external surfaces, because the pore environment stabilizes the molecules and the C-H activation transition states which lowers the activation energy compared to the same type of lattice O-atom in the external surfaces. The rate ratios are high for both MoVTeNb and MoV oxides, suggesting that the unique properties of these oxides may not originate from the presence of Te or Nb.

All M1 phase oxides exhibit $r_{C_2H_6}$ and $r_{C_2H_6}/r_{C_6H_{12}}$ values much higher than VO_x/SiO₂, V₂O₅ and MoO₃, but the differences among the M1 phase oxides are also significant. For example, the $r_{C_2H_6}$ and $r_{C_2H_6}/r_{C_6H_{12}}$ values on the MoVO sample are 16 and 2.5 times the corresponding

values on the MoVTeNbO sample (Fig. 6). Next, we examine the effects of internal micropore areas and external surface areas on these rates and rate ratios to distinguish the effects of these structural properties from the intrinsic reactivity differences.

3.3 Effects of micropore internal areas and external surface areas on C_2H_6 rates and C_2H_6/C_6H_{12} rate ratios

Figure 7a shows the C₂H₆ activation rate per V atom on MoVTeNbO, H₂O₂ treated MoVTeNbO, MoVO, and MoVTeNbO-ht samples as a function of internal micropore area per V atom on these samples derived from N₂ and CO₂ uptakes, as shown in Table 3. The internal areas from CO₂ uptake are higher than N₂ for some samples due to smaller size of CO₂ and higher measurement temperature for the uptake which may help overcome some diffusional constraints [49]. The C₂H₆ activation rate on H₂O₂ treated MoVTeNbO sample is about five times that in untreated MoVTeNbO (Fig. 7a), despite similar elemental composition in the two oxides (Table 2), which is consistent with the increase in micropore volume with H₂O₂ treatment (Table 3). The rates in the different forms of MoVTeNbO samples increase nearly linearly with micropore areas (Fig. 7a), consistent with similar V:Mo ratios (0.23-0.27, Table 3) and small compositional differences and the reactivity differences that can be explained by micropore volumes because C₂H₆ activations occur predominantly inside these micropores. In contrast, the rates on MoVO samples are much higher than the values predicted by the trends for MoVTeNbO samples (Fig. 7a), which suggests that the compositional differences make MoVO intrinsically much more reactive than MoVTeNbO. The higher V:Mo ratio (0.52, Table 3) and the absence of less reducible metals such as Nb form the lattice likely makes the MoVO sample more reactive.

Figure 7b shows C₂H₆/C₆H₁₂ activation rate ratios on MoVTeNbO, H₂O₂ treated MoVTeNbO, MoVO, and MoVTeNbO-ht samples as a function of internal/external area ratios, based on internal micropore areas from N₂ and CO₂ uptakes and external BET areas from N₂ uptakes, as shown in Table 3. The overall lack of a clean linear relation between rate ratios and area ratios suggests that the trends are influenced by possible differences in internal and surface compositions and their effect on reactivity or inaccuracies of physisorption probes. The rate ratios span a much smaller range of values than C₂H₆ activation rates, which are more sensitive to these effects. Nonetheless, the near linear effects of area ratios on rate ratios are more apparent when

internal areas are based on CO₂ uptakes (open symbols in Fig. 7b), because the N₂ based internal areas are more prone inaccuracies [49, 51]. The higher micropore internal areas on H₂O₂ treated MoVTeNbO than on MoVTeNbO is concomitant with higher external surface areas (Tale 3), which leads to similar rate ratios (Fig. 7b) despite five-fold higher C₂H₆ rates in the H₂O₂ treated sample. Similarly, the higher intrinsic reactivity for C₂H₆ in MoVO samples (Fig. 7a) are normalized by concomitant higher reactivity for C₆H₁₂, leading to rate ratios nearly consistent with area ratios (Fig. 7b).

Taken together these data show that the MoV samples exhibit much higher intrinsic reactivity for C-H activation than MoVTeNb samples, and that micropore volumes and external surface areas play an important role in relative rates of reactions at internal and external lattice O-atoms. Next, we assess the effects of structure and composition of monometallic oxides and M1 phase mixed oxides on C-H bond activation energies and product selectivities.

3.4 C-H activation energies for C_2H_6 and C_6H_{12} on monometallic and mixed oxides

3.4.1 Mechanistic interpretations of measured rates

Scheme 2 shows typical elementary steps for oxidative dehydrogenation of saturated hydrocarbons (C_xH_y) on oxides via Mars-van Krevelen redox catalytic cycles with the quasi-equilibrated hydrocarbon adsorption, irreversible C-H activations at lattice O-atoms, H₂O desorption, and O₂ activation. These steps, in the absence of significant gas-phase H₂O or other products lead to the following rate equation [23]:

$$\frac{r_{ODH}}{[M]} = \frac{k_{ODH} K_{ads} P_{C_x H_y}}{1 + K_{ads} P_{C_x H_y} + \frac{k_{ODH} K_{ads} P_{C_x H_y}}{2k_{ox} P_{O_2}}}$$
(2)

where, K_{ads} represents the equilibrium constant for hydrocarbon adsorption, k_{ODH} and k_{ox} represent rate constants for C-H and O₂ activations, respectively, and $P_{C_xH_y}$ represents pressures of hydrocarbons C₂H₆ or C₆H₁₂. The denominator terms represent the ratio of concentrations of unoccupied lattice O-atoms (MO*), adsorbed hydrocarbons, and reduced centers to the MO* concentrations in their respective order of appearance in the equation.

Equation 2 assumes that rates are free from product inhibition, which is consistent with negligible product inhibitions typically observed in C₂H₆-O₂ reactions on oxides [23, 55]. However, recent studies for C₆H₁₂ activation showed some decrease in rates with increasing

residence time, suggesting that product inhibition is significant when measurements were performed at 3 kPa C₆H₁₂ feed at 648K because some oxygenates formed in side reactions may bind strongly to oxide surfaces. Here, the measurements are instead performed at pressures below 0.5 kPa C₆H₁₂, which significantly decreases the product build-up at similar low conversions and minimizes inhibition effects. The effect of conversion changes due to changes in residence times on C₆H₁₂ activation rates on MoVO and MoVTeNb samples is shown in Supporting Information (Fig. S2), which suggests that the product inhibition is negligible at these conditions.

The numerator term in Equation 2 shows a linear dependence of ODH rates on alkane pressures if unoccupied lattice oxygens are the most abundant surface species (MASI), while the denominator terms suggest that high alkane and low O_2 pressures can cause sub-linear alkane pressure dependence by increasing coverages of adsorbed C_xH_y species and reduced centers, respectively, relative to the lattice oxygens. The C_2H_6 activation rates are invariably first-order in C_2H_6 pressure and zero-order in O_2 pressure for conditions relevant to the measurements in this work due to weak alkane binding ($K_{ads}P_{C_2H_6}$ << 1) and rapid nature or re-oxidation steps ($k_{ox}P_{O_2} >> k_{ODH}K_{ads}P_{C_2H_6}$) [23]. The C_6H_{12} activation rates, however, show sublinear $P_{C_6H_{12}}$ and non-zero P_{O_2} dependencies at $P_{C_6H_{12}} >> 1$ kPa and $P_{O_2} << 3$ kPa [23]. In order to minimize such coverage effects, the measurements are performed here at low C_6H_{12} pressures.

Figure 8 shows C₂H₆ and C₆H₁₂ ODH rates on M1 phase MoVO catalysts as a function of C₂H₆ and C₆H₁₂ pressures (648 K, 0-5 kPa C₂H₆ or 0.1-0.5 kPa C₆H₁₂, 3 kPa O₂, 30 cm³ min⁻¹). Both C₂H₆ and C₆H₁₂ rates change linearly with corresponding alkane pressure, which is consistent with insignificant coverage of adsorbed species and reduced centers, and lattice oxygens as the MASI. At these conditions, Equation 2 simplifies to the following form:

$$\frac{r_{ODH}}{[M]} = k_{ODH} K_{ads} P_{C_x H_y} \tag{3}$$

where the first order rate constant can be obtained by dividing the measured rate by C_2H_6 or C_6H_{12} pressure. These measured rate constants represent the Gibbs free energy of C-H activation transition state (G^{\ddagger}) relative to bare lattice oxygens (G_{MO^*}) and gaseous molecules ($G_{C_xH_{y(g)}}$):

$$k_{ODH}K_{ads} \sim e^{\frac{-\Delta G^{\ddagger}}{RT}} = e^{\frac{-(G^{\ddagger} - G_{MO*} - G_{C_{\chi}H_{y}(g)})}{RT}}$$
 (4)

The enthalpy and entropy contributions from the Gibbs free energy change in Equation 4 ($\Delta G^{\dagger} = \Delta H^{\dagger} - T\Delta S^{\dagger}$) is given by the Eyring-Polanyi equation [56]:

$$\ln\left(\frac{k_{ODH}K_{ads}h}{k_{B}T}\right) = \frac{\Delta S^{\ddagger}}{R} - \frac{\Delta H^{\ddagger}}{RT}$$
 (5)

where, h and k_B represent the Planck and Boltzmann constants, respectively.

3.4.2 Effects of structure and composition on C-H activation enthalpy and entropy

Table 4 shows $k_{ODH}K_{ads}$ values on VO_x/SiO₂, MoO₃, MoVTeNbO, H₂O₂ treated MoVTeNbO, and MoVO for C₂H₆ at 648-773K and C₆H₁₂ at 588-673K and the corresponding $\ln \left(\frac{k_{ODH}K_{ads}h}{k_BT}\right)$ values as a function of reciprocal temperature are shown in Figure 9. The activation enthalpy and entropy values given by equation 5 and the slopes and intercepts in Figure 9 are shown in Table 5.

The C₂H₆ activation enthalpy on 11 wt.%VO_x/SiO₂ sample is much higher than the enthalpy on te 41 wt.% VO_x/SiO₂ sample that predominantly contains V₂O₅ nanoparticles (105±15 and 78±10 kJ mol⁻¹, Table 5), which is consistent with higher reactivity in the nanoparticles. The activation energy for the unsupported MoO₃ sample is higher than both VO_x/SiO₂ samples (116±12 kJ mol⁻¹, Table 5), consistent with the much lower reactivity of Mo than V. The calculated HAE values in our previous study [23] for both bridging and terminal O-atoms connected to Mo were more positive than the respective O-atoms connected to V-atoms, which confirms that O-atoms connected to Mo-atoms are weaker abstractors than the O-atoms connected to V-atoms. The C₂H₆ activation enthalpy in untreated MoVTeNbO and MoVTeNbO-ht samples are similar to 41 wt.% VO_x/SiO₂, while that in H₂O₂ treated MoVTeNbO and MoVO are slightly lower. The lower enthalpy is consistent with higher intrinsic reactivity of the MoVO sample.

The C₆H₁₂ activation enthalpies are lower than C₂H₆ on all oxide samples, which is consistent with the weaker C-H bonds in C₆H₁₂ (Table 5). The C₆H₁₂ activation enthalpies on M1 phase oxides are higher than VO_x/SiO₂ samples (70±14, 63±13, 64±9 and 40±17 kJ mol⁻¹ for MoVTeNbO, H₂O₂ treated MoVTeNbO, MoVO, and VO_x/SiO₂, respectively), which suggests that lattice O-atoms in M1 phase oxides are less reactive than V₂O₅. The $\Delta H_{C_2H_6} - \Delta H_{C_6H_{12}}$ values are about 38-72 kJ mol⁻¹ on VO_x/SiO₂, and MoO₃ due to weaker bonds in C₆H₁₂, but only 3-13 kJ mol⁻¹ in M1 phase oxides because the effects of stronger C-H bonds in C₂H₆ is partially offset by its stabilization by van der Waals forces within the heptagonal pores of the M1 phase, as shown by DFT calculations [23].

The negative values of the activation entropies in Table 5 represent entropy that the gaseous molecules lose in order to form a transition state on the surface. Unlike the activation enthalpy values, the entropy loss given by Equation 5 sensitive to site normalization, which leads to inconsistent values among low and high surface density VO_x/SiO₂ samples. For high loading VO_x/SiO₂ samples forming large nanoparticles only a small fraction of V-atoms is accessible. Thus, the measured rate constant is much smaller than true rate constant because the measured rates are normalized by all V atoms. This effect of dispersion on rate constants can be given by:

$$(k_{ODH}K_{ads})_{meas} = D(k_{ODH}K_{ads})_{true} \tag{6}$$

where, the dispersion D is the fraction of surface atoms exposed on the surface. Substituting the right-hand side of Equation 6 for the measured rate constant in Equation 5 gives:

$$\ln\left(\frac{(k_{ODH}K_{ads})_{meas}h}{k_{B}T}\right) = \ln\left(\frac{D(k_{ODH}K_{ads})_{true}h}{k_{B}T}\right) = \frac{(\Delta S^{\ddagger})_{meas}}{R} - \frac{\Delta H^{\ddagger}}{RT}$$
Or,
$$\ln\left(\frac{(k_{ODH}K_{ads})_{true}h}{k_{B}T}\right) = \frac{(\Delta S^{\ddagger})_{meas} - Rln(D)}{R} - \frac{\Delta H^{\ddagger}}{RT}$$
(7)

Thus, the measured ΔS^{\ddagger} values are incorrect by -Rln(D), and a D value of 0.1 and 0.01 will make the true values less negative than the values in Table 5 by 19 and 38 J mol⁻¹ K⁻¹, respectively. The measured ΔS^{\ddagger} values for monovanadates in 11 wt.%VO_x/SiO₂ and V₂O₅ nanoparticles in 41% VO_x/SiO₂ samples are -203±21 and -250±15 J mol⁻¹K⁻¹, which suggests that a D value much less than one would make the entropy loss in the two samples similar, as expected for large nanoparticles in the latter catalyst. The measured entropy loss for MoO₃ sample with expected low dispersion is -223 ±17 J mol⁻¹K⁻¹, suggesting that the true dispersion is much less negative. The M1 phase must exhibit larger D values due to pore accessibility, but more negative values of try entropy loss due to pore confinements (Table 5). The effects of site normalization cancel the $\Delta S^{\ddagger}_{C_2H_6} - \Delta S^{\ddagger}_{C_6H_{12}}$ values. These entropy differences are more positive for all catalysts, which suggests that the lighter C₂H₆ molecules lose less entropy to form the transition state due to less entropy in the gas-phase. VO_x/SiO₂ and MoO₃ exhibit more positive $\Delta S^{\ddagger}_{C_2H_6} - \Delta S^{\ddagger}_{C_6H_{12}}$ values than M1 phase catalysts, which is consistent with relatively greater entropy loss for C₂H₆ due to pore confinement.

3.5 Product selectivities for C_2H_6 and C_6H_{12} oxidation on monometallic and mixed oxides

Figure 10a shows C_2H_6 conversion and product selectivity in C_2H_6 -O2 reactions at 648K, 3 kPa C_2H_6 , 3 kPa O_2 , and 30 cm³ min⁻¹ on VO_x/SiO_2 and MoO_3 and M1 phase oxides. The MoVTebO, H_2O_2 treated MoVTebO and MoVO oxides exhibit much higher selectivity to C_2H_4 (96, 96, and 95% $S_{C_2H_4}$ at 1.2, 2.4, and 5.4% $X_{C_2H_6}$, respectively) than oxides without micropores (54 and 56% $S_{C_2H_4}$ at 0.4% $X_{C_2H_6}$ for VO_x/SiO_2 and MoO_3 , respectively) at similar conversions, which is consistent with the well-known selectivity trends on these materials [23, 57]. The H_2O_2 treatment and changes in the elemental compositions of V, Te, Nb do not alter product selectivity in MoV based oxides but confers significant increases in measured rates due to corresponding increases in micropore volumes and intrinsic reactivity (Figure 4a, 6a). These details, together with high C_2H_6/C_6H_{12} rate ratios indicating that most C_2H_6 activations on M1 phase occurs inside micropores, demonstrate that micropore structure also plays a role in enhancing selectivity which is more significant than the effect of composition of these oxides. The C_2H_4 selectivity for the M1 phase oxides also decreases much less sensitively with conversion than for VO_x/SiO_2 and MoO_3 (Fig. 10b).

Figure 11a shows C_6H_{12} conversion and product selectivity in C_6H_{12} -O₂ reactions on VO_x/SiO_2 , MoO_3 , and M1 phase mixed oxides at 30 cm³ min⁻¹, 0.5 kPa C_6H_{12} , and 3 kPa O₂, 648 K. The selectivity to dehydrogenation products C_6H_{10} and C_6H_6 are similar on VO_x/SiO_2 , MoO_3 , MoVTebO, H_2O_2 treated MoVTebO, and MoVO (1-2% $S_{C_6H_{10}}$ and 55-66% $S_{C_6H_6}$ at 2-8% $X_{C_6H_{12}}$). These trends suggest that the nature of external surfaces of all oxides confer similar selectivity to oxidative dehydrogenation products (C_6H_{10} and C_6H_6) and that the high selectivity to C_2H_4 during C_2H_6 ODH on three MoV oxides originates specifically from some property within the micropores. The sensitivity of product selectivity to conversion is similar on VO_x/SiO_2 , MoVTebO, H_2O_2 treated MoVTebO, and MoVO (Fig. 11b), which contrasts the different trends observed during C_2H_6 conversion.

The effect of conversion on selectivity can be analyzed by analyzing relative values of rate constants for the desired dehydrogenation reaction and the parallel and sequential formation of side products, as shown in Scheme 3. The primary and parallel products (steps with rate constants k_1 and k_2 in Scheme 2) form directly form reactants and their selectivity remains insensitive to conversion. The sequential products form more as more dehydrogenated products build-up at increasing conversions, which leads to change in selectivity with conversion. Mole balances on

reactants and products formed with first-order rates constants gives C₂H₄ selectivity with the following dependence on conversion for C₂H₆ [24]:

$$S_{C_2H_4} = S_{C_2H_4}^0 \left(1 - \frac{1}{2} S_{C_2H_4}^0 \frac{k_3}{k_1} X_{C_2H_6} \right) \tag{8}$$

where, $S_{C_2H_4}^0 = k_1/(k_1 + k_2)$ is the selectivity at zero conversion. Analogous assumptions for C_6H_{12} oxidations lead to selectivity expressions for $C_6H_{10} + C_6H_6$ obtained by replacing $S_{C_2H_4}^0$ with $S_{C_6H_{10}+C_6H_6}^0$ and $X_{C_2H_6}$ with $X_{C_6H_{12}}$ in Equation 8.

Regression of the effect of conversion on selectivity data (Fig. 10b, 11b) to the functional form of Equation 8 gives rate constant ratios k₂/k₁ and k₃/k₁ and smaller values of k₂/k₁ and k₃/k₁ represent higher C₂H₄ selectivity at zero conversion and smaller decrease in selectivity with increasing conversion, respectively. For the data shown in Figure 10b, the k₂/k₁ values are smaller on M1 phase oxides (0.03-0.04) than on VO_x/SiO₂, V₂O₅, and MoO₃ (0.64±0.02, 0.65±0.03 and 0.63±0.03, respectively) as shown in Figure 12a. The measured larger k₂/k₁ values on VO_x/SiO₂, V₂O₅, and MoO₃ represent significant formation of CO_x oxides at zero conversion via parallel reactions. The smaller k₂/k₁ values on M1 phase MoV oxides represent primary C-H activations that are preferred over parallel O-insertion reactions that results in high C₂H₄ selectivity (>95%).

The k₃/k₁ values are much smaller on three MoV oxides (0.4±0.1, 0.4±0.1, and 0.5±0.1 for MoVTeNbO, H₂O₂ treated MoVTeNbO, and MoVO, respectively) than on VO_x/SiO₂ (92±8), V₂O₅ (77±15), and MoO₃ (70±12). These values suggest that non-microporous oxides favor sequential over primary reactions that lead to a significant decrease in C₂H₄ selectivity with increasing C₂H₆ conversion. In addition, k₃/k₁ values are much larger than k₂/k₁ on all oxide catalysts that implies the sequential reactions suppress the C₂H₄ selectivity more significantly than parallel reactions. Thus, on MoVTeNbO, H₂O₂ treated MoVTeNbO, and MoVO, the smaller rates of parallel and sequential O-insertion steps (k₂ and k₃ in Scheme 1a) relative to the desirable dehydrogenation step (k₁) in C₂H₆ ODH are observed. In contrast, the k₂/k₁ (0.4-0.7) and k₃/k₁ (1-2) values of C₆H₁₂ ODH are similar on all oxide samples as shown in Figure 12b. These similar selectivity trends and rate constant ratios on different compositions of MoV oxides suggest that the high C₂H₄ selectivity originates specifically from the micropores. We conclude that the unique property of micropores of MoV based oxides originates from the vdW stabilization of tightly confined C₂H₆ and C₂H₄, and resistance to O-insertion due to shape and curvature of micropores.

4. Conclusions

The role of the microporous structure of M1 phase MoV oxides on reactivity and selectivity in alkane ODH reactions are elucidated by measured ratios of C₂H₆ to C₆H₁₂ activation rates and ratios of sequential or parallel to primary reactions rate constants on microporous MoV oxides as well as on non-microporous V₂O₅ and MoO₃. Treatment of MoVTeNbO with H₂O₂ improves the purity of the desired M1 phase through the dissolution of the intergrown M2 phase and results in substantial decreases in bulk Te content and two-fold enhancements in the accessibility of both internal micropores and external surfaces. Furthermore, hydrothermal synthesis of MoVO without Te and Nb lead to slightly increased accessible micropore volumes and similar external surfaces areas compared to those of H₂O₂ treated MoVTeNbO. These differences in bulk elemental compositions and accessible micropore volumes among MoVTeNbO, H₂O₂ treated MoVTeNbO, and MoVO are further examined to probe the origin of high selectivity in M1 phase oxides.

The ratios of C₂H₆ to C₆H₁₂ activation rates on MoVTeNbO, H₂O₂ treated MoVTeNbO, and MoVO are all close to unity and are of two orders of magnitude higher than the ratios measured on non-microporous unsupported and supported V₂O₅ and MoO₃ oxides. These observed low ratios on both V₂O₅ and MoO₃ suggest that measured ratios are less sensitive to H-abstractor strength of O-atoms connect to Mo or V atoms. In addition, rate ratios on supported VO_x/SiO₂ (1.5-41% wt.) and unsupported V₂O₅ are similar and much less than unity which implies that the measured ODH rate ratios are independent of dispersion and associated structural changes of VO_x domains. Therefore, the measured high C₂H₆ to C₆H₁₂ ODH ratios on M1 phase MoV oxides strongly suggest the importance of micropores in ethane activation which is consistent with conclusions from our previous study [23]. The ethane activation rates increase with increasing internal micropore areas among the MoV oxides explored in this study. This trend further suggests that increases in internal micropore areas increase the number of accessible active sites for ethane activation. Moreover, the observed high ethane activation rates on MoVO among the three M1 phase oxides indicate that Te atoms are insignificant and hence are not necessary for the active site structure, which is in contrast to some previous claims [58]. Furthermore, ratios of C₂H₆ to C₆H₁₂ activation rates scale linearly with the ratios of internal micropore to external surface areas on these MoV oxides.

The observed first and zero order dependences of alkane ODH rates on alkane pressure and dioxygen pressure respectively are consistent with the kinetically relevant C-H activation steps based on Mars-van Krevelen redox catalytic cycles. The activation enthalpy differences between C₂H₆ and C₆H₁₂ are much higher for non-microporous V₂O₅ and MoO₃ oxides (above 45 kJ mol⁻¹) than microporous MoV oxides (around 10 kJ mol⁻¹) which is consistent with our previous suggestions of the stabilization of C₂H₆ molecules by vdW interactions with micropore walls.

The effects of conversion on C₂H₄ selectivity show that non-microporous oxides of vanadium and molybdenum (VO_x/SiO₂, V₂O₅ and MoO₃) exhibit larger rate constant ratios of parallel oxidation to primary dehydrogenation reactions (k₂/k₁) than those on M1 phase MoV oxides [24]. The high k₂/k₁ ratios resulted in low C₂H₄ selectivity and significant CO_x selectivity at zero conversion on non-microporous oxides while low ratios represent high C₂H₄ selectivity and no CO_x formation at zero C₂H₆ conversion on M1 phase MoV oxides. Similarly, non-microporous oxides exhibit larger rate constant ratios of sequential oxidation to primary dehydrogenation reactions (k₃/k₁) compared to M1 phase MoV oxides. The high ratios of k₃/k₁ represent a significant decrease in C₂H₄ selectivity with increasing conversion on non-microporous oxides while low ratios on M1 phase MoV oxides represent high C₂H₄ selectivities which are less sensitive to conversion. In all, these ratios suggest that microporous oxides of M1 phase are highly selectivity for C₂H₄ formation and are independent of bulk elemental compositions. In contrast, the effect of C₆H₁₂ conversion on the sum of C₆H₁₀ and C₆H₆ selectivity shows that k₂/k₁ and k₃/k₁ are similar on all oxide catalysts, which suggest that external surfaces of all oxides are similarly active for primary, parallel, and sequential reactions. Thus, this study further elucidates the direct role of heptagonal pores in controlling rates and selectivity to alkene products during alkane ODH reactions.

Author Information Corresponding Author

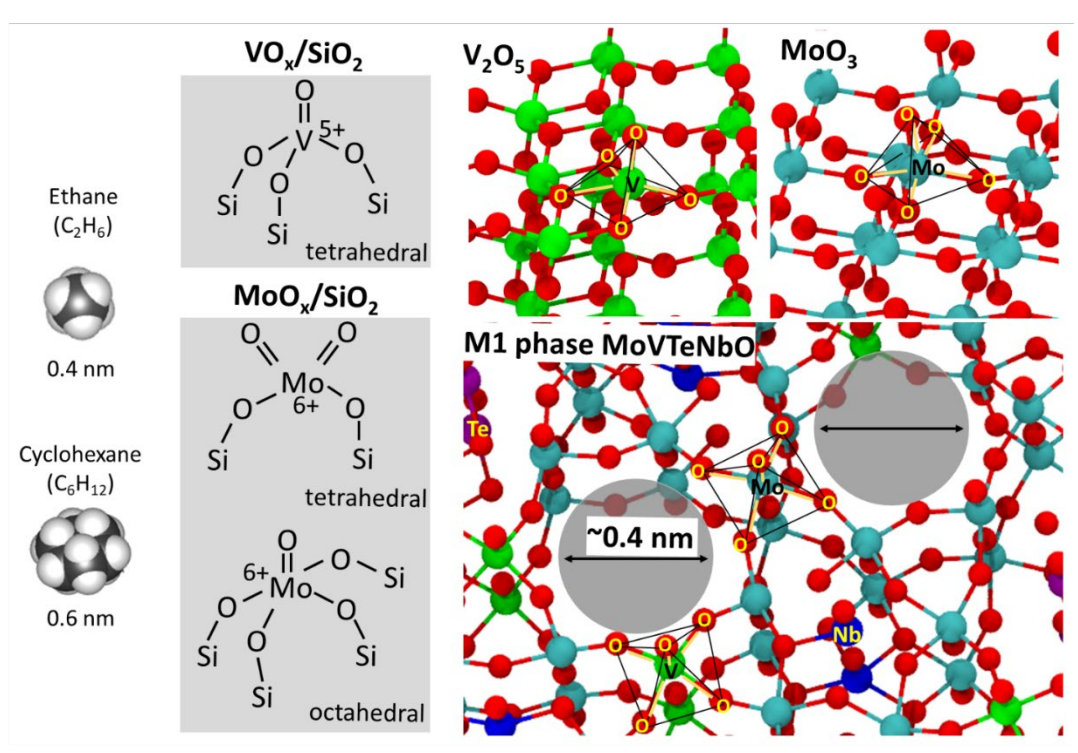
*P.D., Phone: +1-617-627-7972, Fax: +1-617-627-3991

Email address: prashant.deshlahra@tufts.edu.

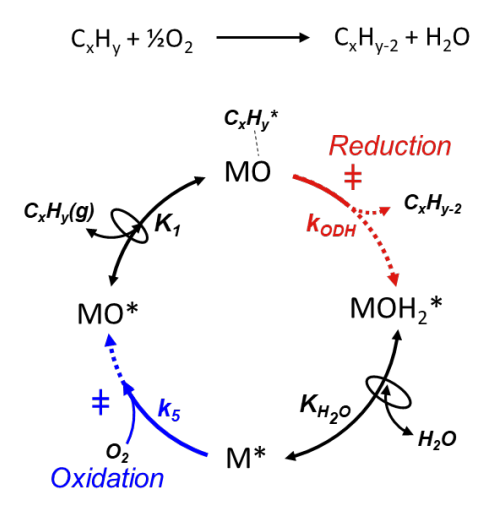
*S.L.S., Phone: +1-860-486-2797 Email address: steven.suib@uconn.edu

Acknowledgements

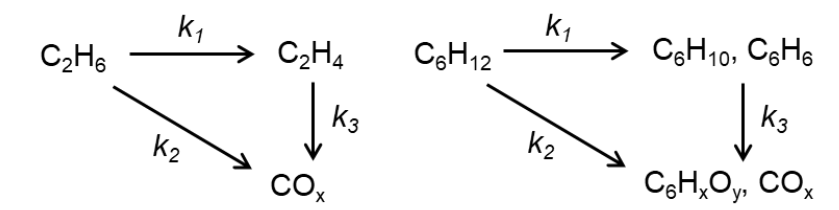
Financial support was provided National Science Foundation (award number 1803798) and Tufts Collaborates. Partial support from ACS PRF (award number 57869-DNI5) is also acknowledged.



Scheme 1. Structures of molecules and oxides.



Scheme 2. Elementary steps for oxidative dehydrogenation of alkanes and cycloalkanes mediated by redox cycles in transition metal oxides.



Scheme 3. Rate constants representing dehydrogenation of alkanes or cycloalkanes (k_1) and their conversion to oxygenated products via parallel conversion of alkanes or alkanes (k_2) and sequential conversion of dehydrogenated products (k_3).

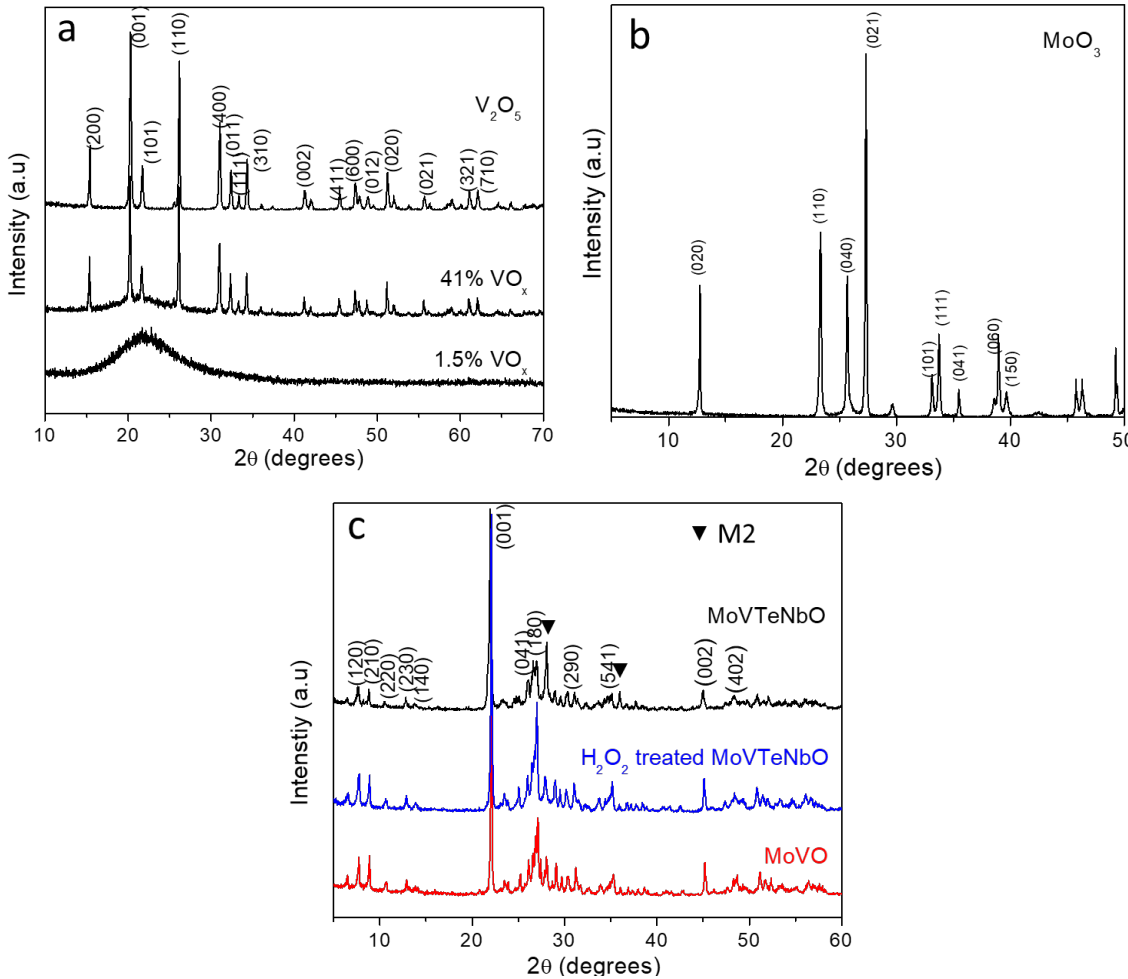


Figure 1. XRD patterns of (a) 1.5 and 41 wt.% VO_x/SiO_2 , and V_2O_5 , (b) MoO₃, and (c) MoVTeNbO, H₂O₂ treated MoVTeNbO, and MoVO. Miller indices correspond to orthorhombic V_2O_5 , MoO₃ and M1 phases in (a), (b) and (c), respectively.

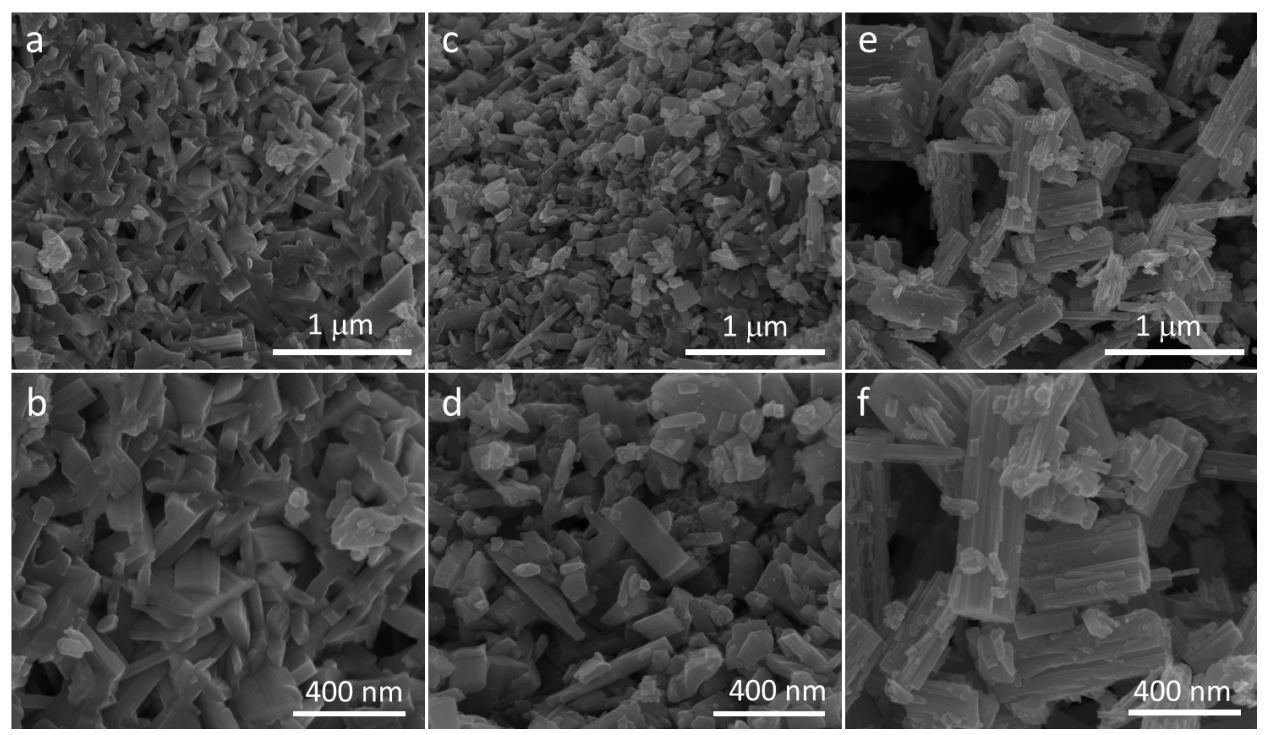


Figure 2. SEM images of ground (a,b) MoVTeNbO, (c,d) H₂O₂ treated MoVTeNbO, and (e,f) MoVO samples.

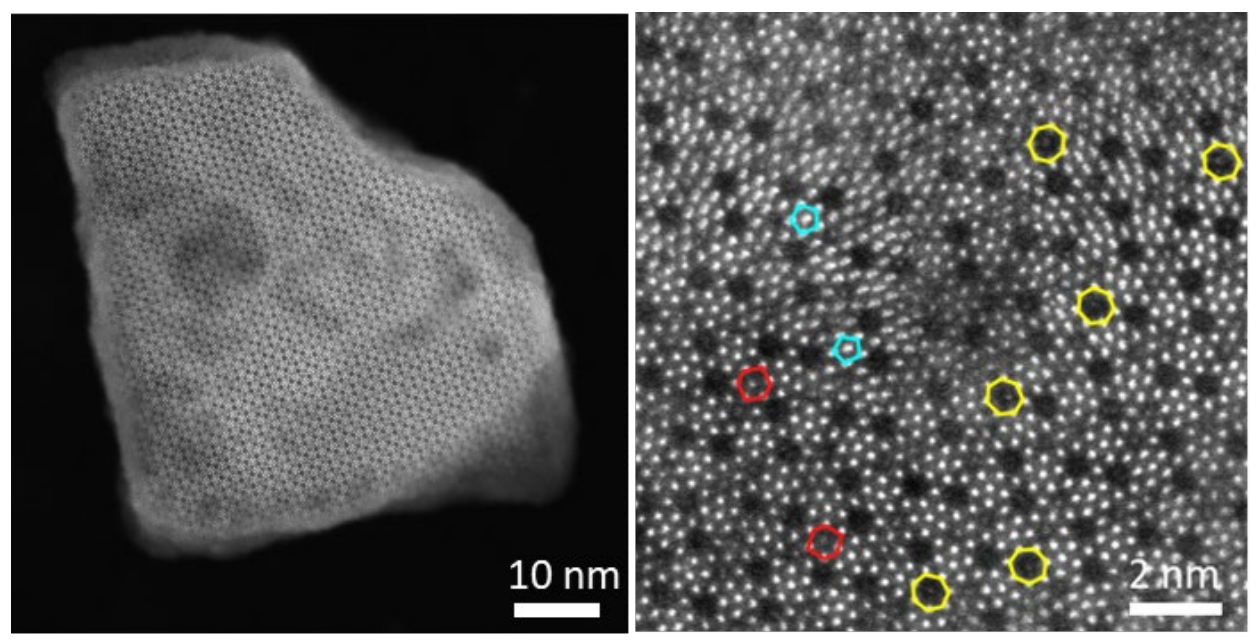
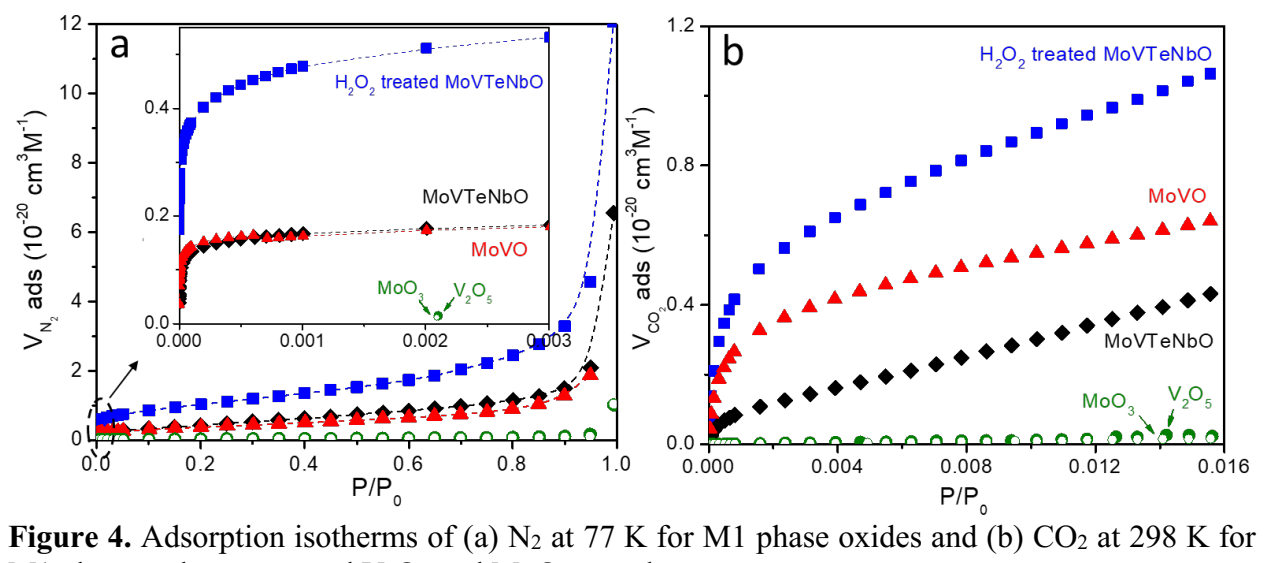


Figure 3. HAADF-STEM images of (001) planes on H₂O₂ treated MoVTeNbO. Cyan, red and yellow polygons mark some of the pentagonal, hexagonal and heptagonal channels rings, respectively.



M1 phase and unsupported V₂O₅ and MoO₃ samples.

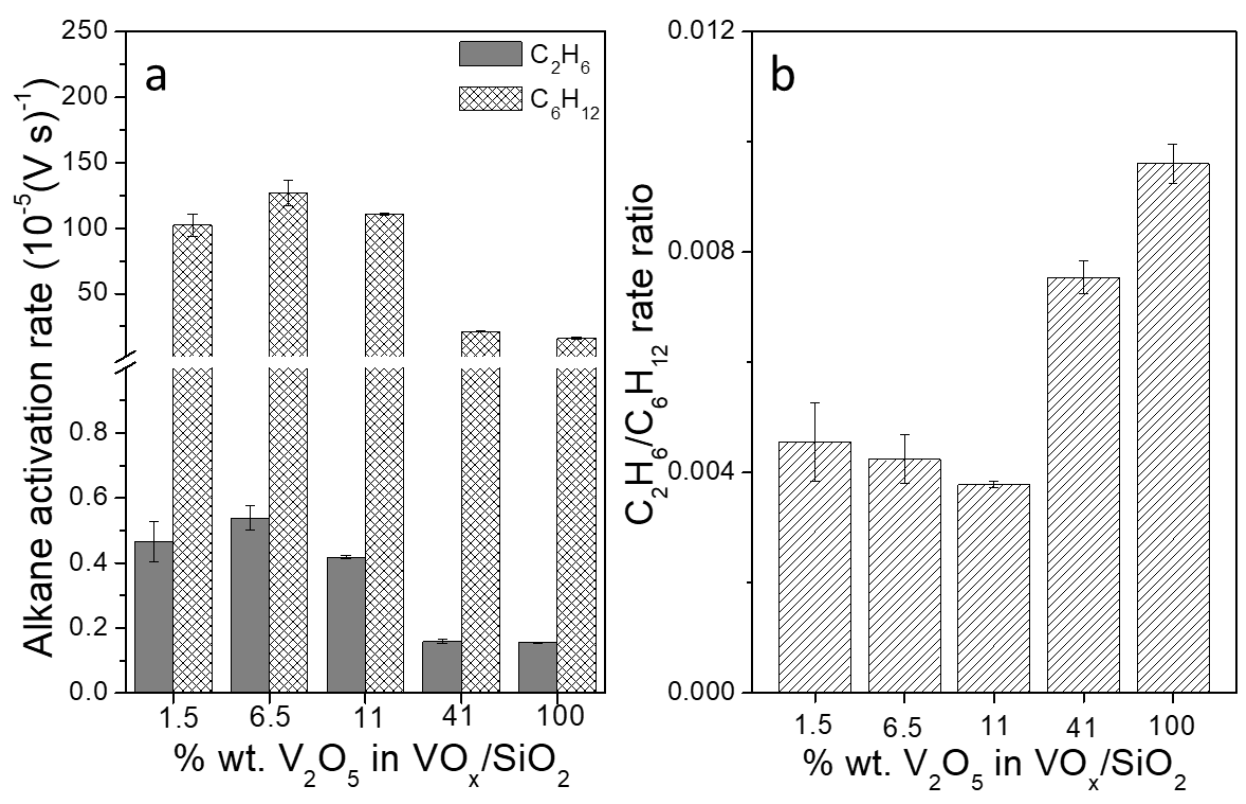


Figure 5. Measured (a) C_2H_6 and C_6H_{12} activation rates and (b) C_2H_6/C_6H_{12} rate ratios, on 1.5, 6.5, 11, and 41% wt. VO_x/SiO_2 , and unsupported V_2O_5 , at 648 K, 3 kPa C_2H_6 or C_6H_{12} , 3 kPa O_2 , 30 cm³ min⁻¹ (0.04, 0.14, 0.53, 0.92, 0.47 % C_2H_6 and 4, 5, 5, 8, 5 % C_6H_{12} conversions). Uncertainties represent standard deviation in initial rates.

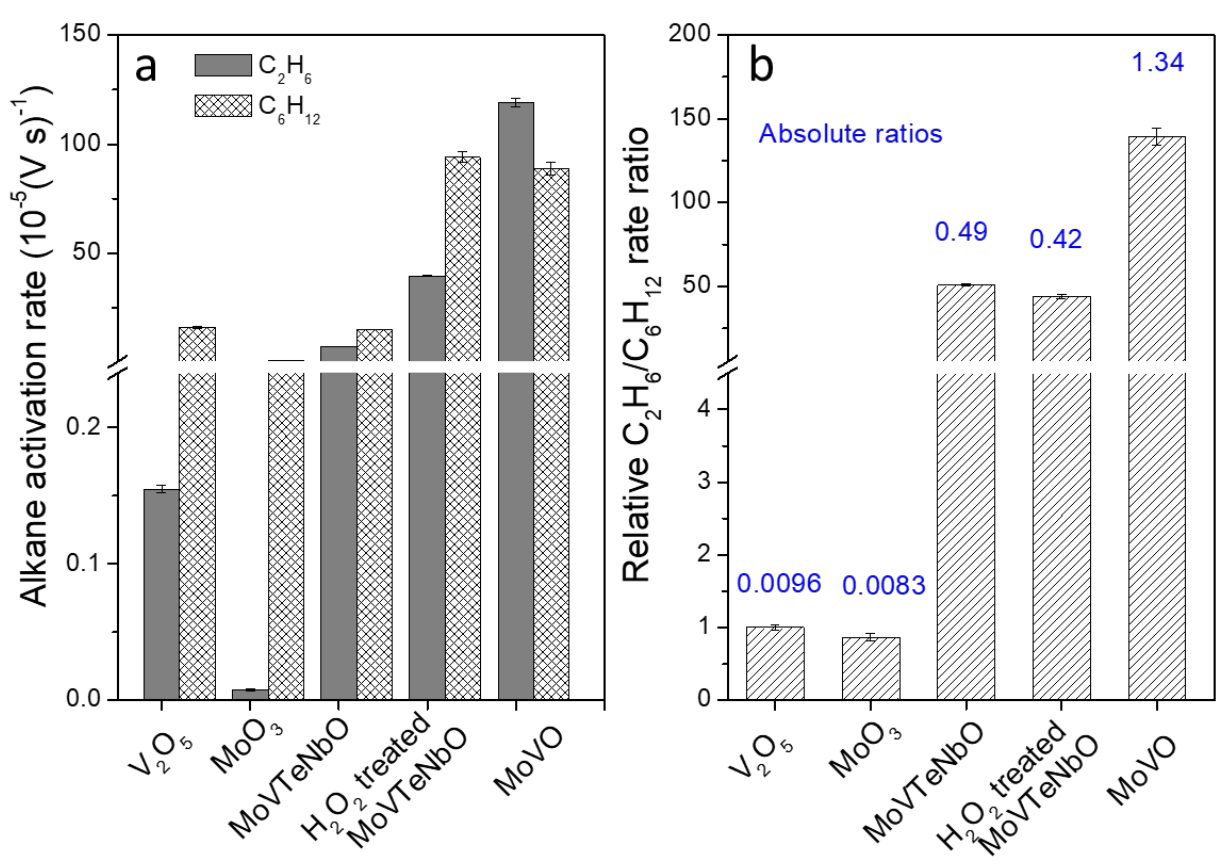


Figure 6. Measured (a) C_2H_6 and C_6H_{12} activation rates on V_2O_5 , MoO_3 and M1 phase oxides, and (b) C_2H_6/C_6H_{12} rate ratios on these oxides relative to the ratio on V_2O_5 sample (648 K, 3 kPa C_2H_6 or C_6H_{12} , 3 kPa O_2 , 30 cm³ min⁻¹; 0.4, 0.1, 1.2, 2.2 and 5.7% C_2H_6 and 2.3, 2.5, 2.9, 5.0 and 4.4% C_6H_{12} conversions on V_2O_5 , MoO_3 MoVTeNbO, H_2O_2 treated MoVTeNbO and MoVO, respectively). Uncertainties represent standard deviation in initial rates.

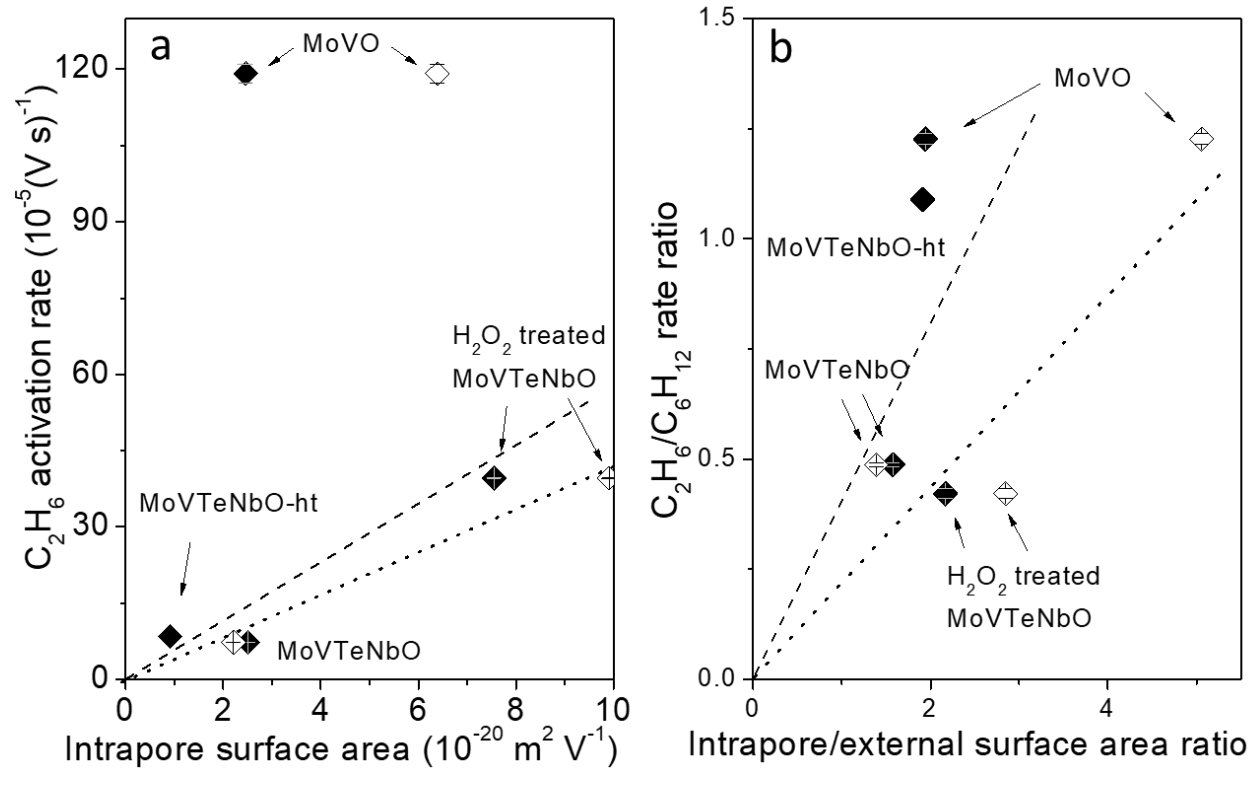


Figure 7. Measured (a) C₂H₆ activation rates as a function of intrapore surface area and (b) C₂H₆/C₆H₁₂ rate ratios as a function of internal micropore to external surface area ratio, on MoVTeNbO, H₂O₂ treated MoVTeNbO and MoVO (648 K, 3 kPa C₂H₆ or C₆H₁₂, 3 kPa O₂, and 30 cm³ min⁻¹). Closed and open symbols represent internal areas derived from N₂ and CO₂ uptakes, respectively. Dashed and dotted lines are added to guide the eye for deviations from linearity for intrapore areas based on N₂ and CO₂ uptakes, respectively. Uncertainties represent standard deviation in initial rates.

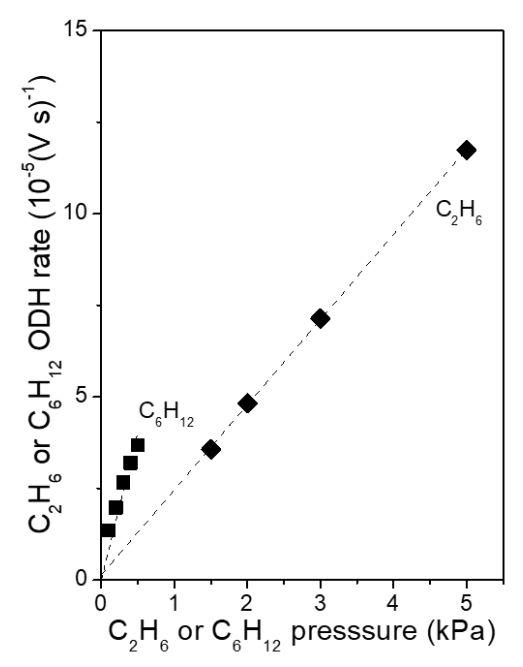


Figure 8. Measured C_2H_6 and C_6H_{12} ODH rates on MoVTeNbO as a function of corresponding alkane pressure at 648 K, 3 kPa O_2 , and 30 cm³ min⁻¹. Dashed lines represent best linear fits.

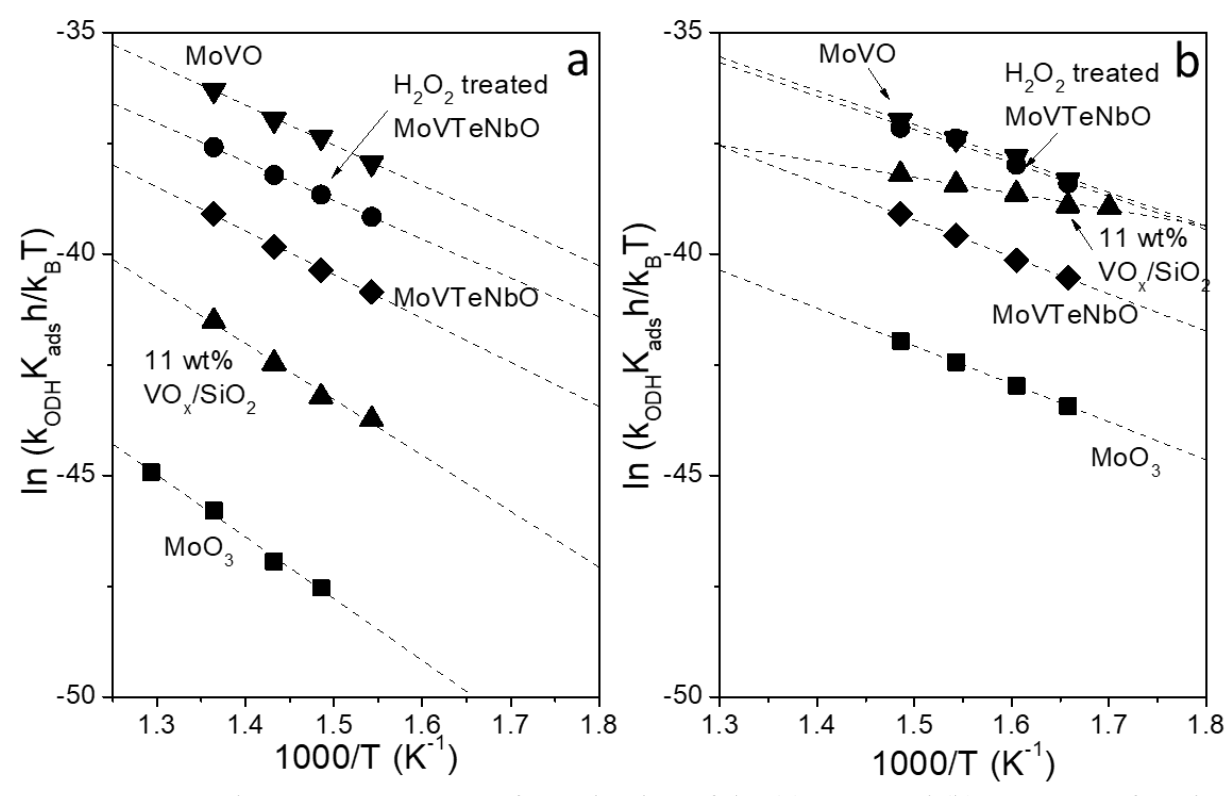


Figure 9. Measured ODH rate constants for activation of the (a) C_2H_6 and (b) C_6H_{12} as a function of reciprocal temperature on VO_x/SiO_2 (triangles), MoO_3 (squares), MoVTeNbO (diamonds), H_2O_2 treated MoVTeNbO (circles) and MoVO (inverted triangles). Dashed lines represent linear regression fits to form of Equation 10. Reaction conditions: 588-773 K, 3 kPa C_2H_6 or 0.5 kPa C_6H_{12} , 3 kPa O_2 , and 30 cm³ min⁻¹.

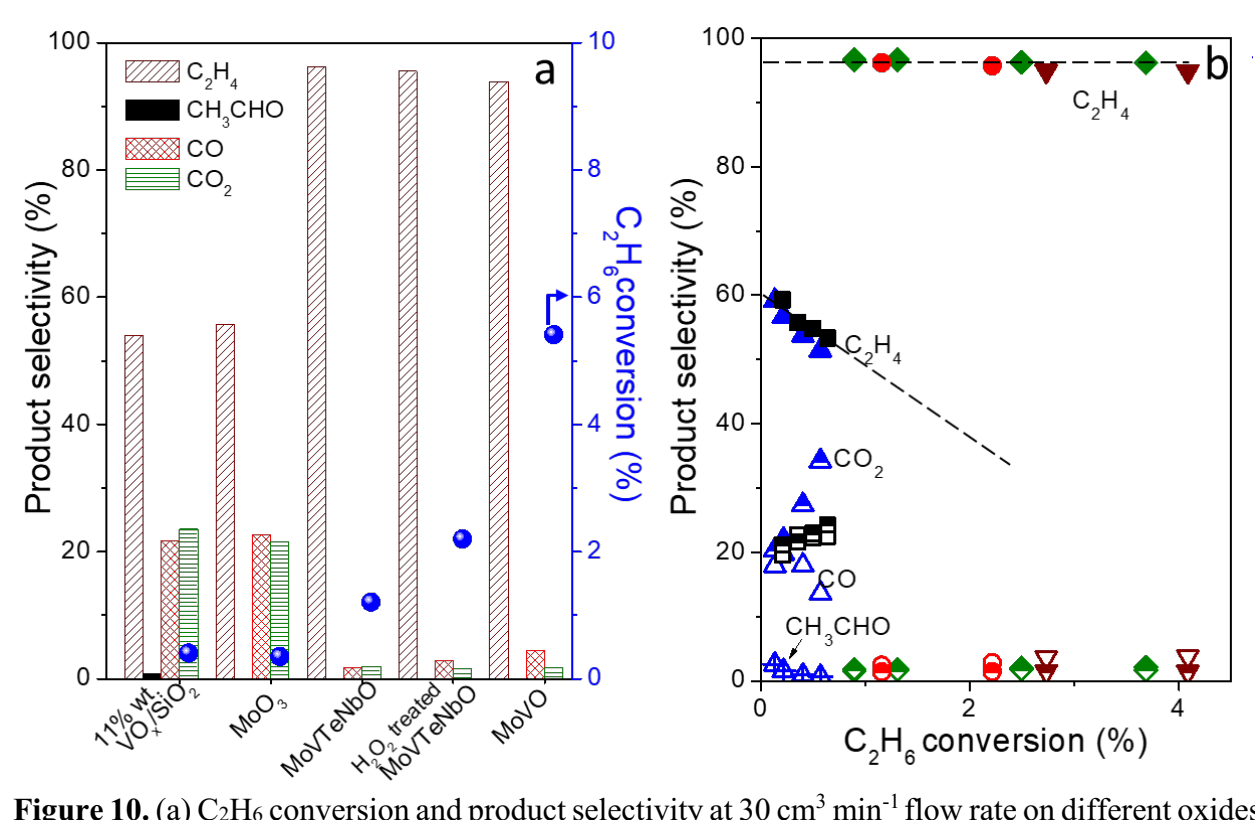


Figure 10. (a) C₂H₆ conversion and product selectivity at 30 cm³ min⁻¹ flow rate on different oxides and (b) C₂H₄ (closed symbols), CH₃CHO (cross symbols), CO (open symbols) and CO₂ (half-open symbols) selectivity as a function of conversion on 11% wt. VO_x/SiO₂ (triangles), MoO₃ (squares), MoVTeNbO (diamonds), H₂O₂ treated MoVTeNbO (circles) and MoVO (inverted triangles), at 648 K, 3 kPa C₂H₆, 3 kPa O₂. Dashed curve to guide the eye for changes in C₂H₄ selectivity as a function of conversion.

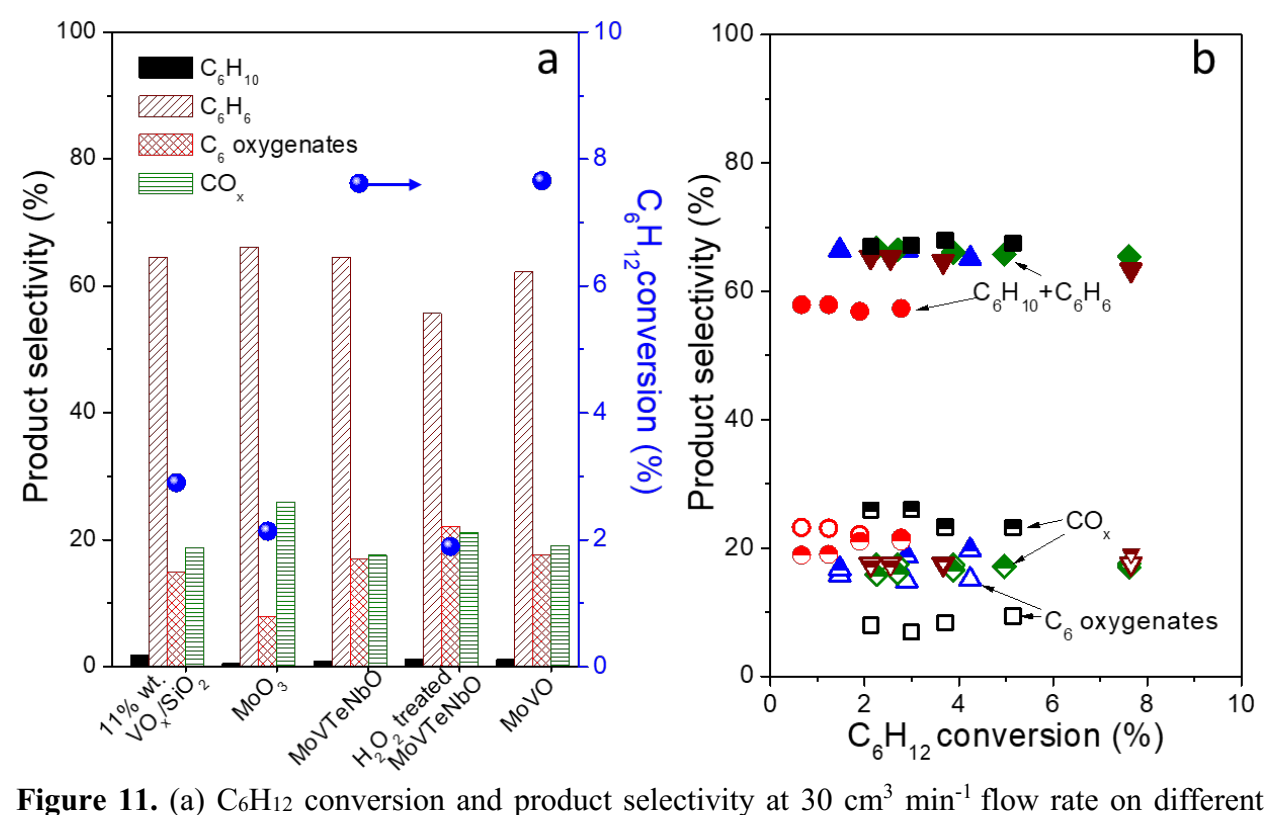


Figure 11. (a) C₆H₁₂ conversion and product selectivity at 30 cm³ min⁻¹ flow rate on different oxides and (b) C₆H₁₀+C₆H₆ (closed symbols), C₆ oxygenates (open symbols) and CO_x (half-open symbols) selectivity as a function of conversion on 11% wt. VO_x/SiO₂ (triangles), MoO₃ (squares), MoVTeNbO (diamonds), H₂O₂ treated MoVTeNbO (circles) and MoVO (inverted triangles), at 648 K, 0.5 kPa C₆H₁₂, 3 kPa O₂.

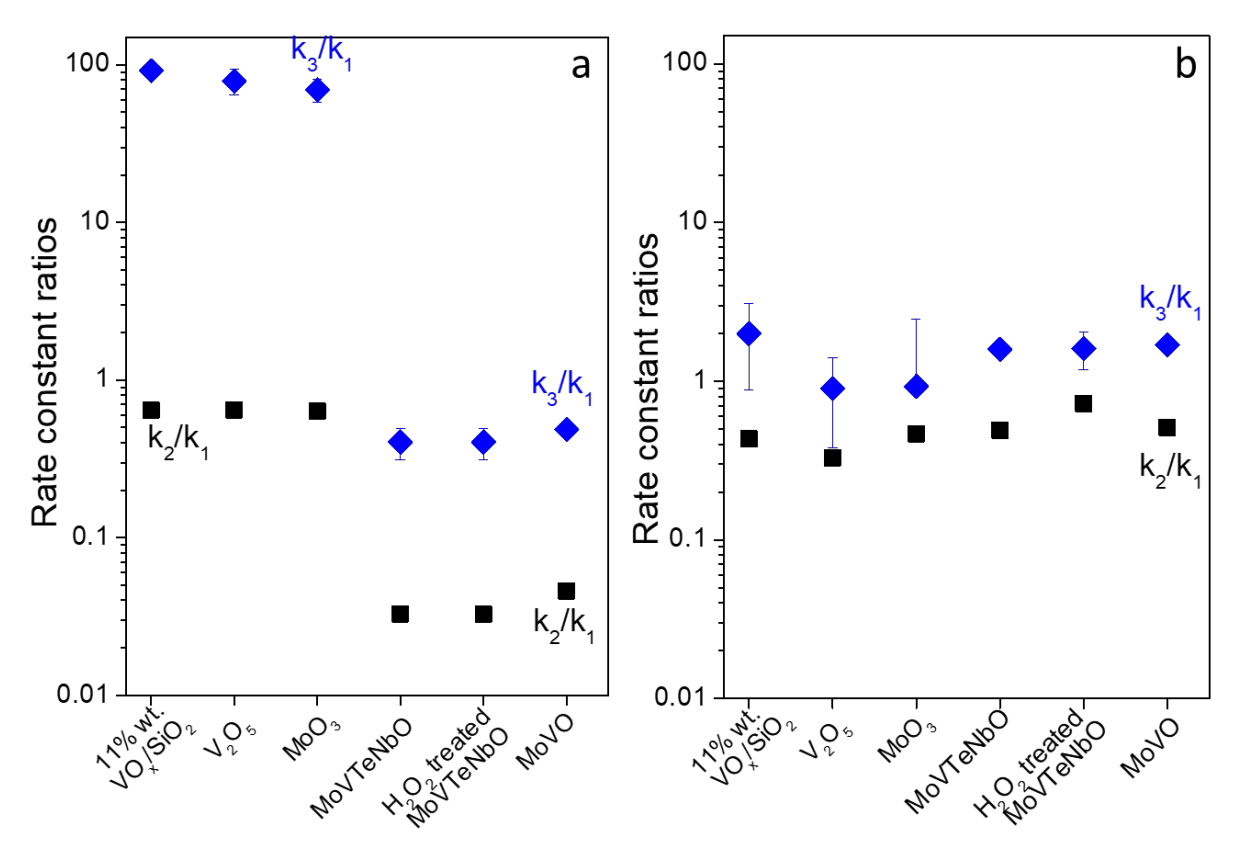


Figure 12. Rate constant ratios representing parallel and sequential reactions relative to the dehydrogenation of (a) C₂H₆ and (b) C₆H₁₂ on monometallic oxides and M1 phase mixed oxides at 648 K, 3 kPa C₂H₆ or 0.5 kPa C₆H₁₂, 3 kPa O₂. Uncertainties represent standard errors.

Table 1. Compositions, surface densities and surface areas in VO_x/SiO₂ and unsupported V₂O₅

and MoO3 samples.

V ₂ O5 wt. % in VO _x /SiO ₂ ^a	Theoretical surface density on SiO ₂	Weight per V or Mo	External surface area		
, o _x 010 ₂	(V nm ⁻²)	(g mol-V ⁻¹) or (g mol-Mo ⁻¹)	$(m^2 g^{-1})$	$(10^{-20} \text{ m}^2 \text{ V}^{-1}) \text{ or}$ $(10^{-20} \text{ m}^2 \text{ Mo}^{-1})^b$	
1.5	0.2	6062.6	245.6	247.2	
6.5	1.0	1399.1			
11	1.7	826.7			
41	9.6	221.8	35.3	1.3	
Unsupported V ₂ O ₅		181.88	8.1	0.12	
Unsupported MoO ₃		143.9	4.5	0.11	

^a Measured using ICP-AES

Table 2. Measured bulk elemental composition and weight of sample per mole of V atoms.

Catalyst	Mo/V/Te/Nb atomic ratio ^a	Weight per V (g mol-V ⁻¹) ^b
MoVTeNbO	1/0.23/0.25/0.17	977.9
H ₂ O ₂ treated MoVTeNbO	1/0.24/0.12/0.23	908.1
MoVO	1/0.52	365.5
MoVTeNbO-ht ^c	1/0.27/0.02/0.09	687.0

^a Measured using ICP-AES

Table 3. Internal micropore and external surface areas using N_2 and CO_2 uptake measurements on M1 phase oxides.

Titl primot orritor								
Catalyst -	Gas volume uptake ^a		Intrapore surface area ^b				External surface area	
	N_2	CO_2	N_2		CO ₂			
	(cm	³ g ⁻¹)	$(m^2 g^{-1})$	$(10^{-20} \text{ m}^2 \text{ V}^{-1})^c$	$(m^2 g^{-1})$	$(10^{-20} \text{ m}^2 \text{ V}^{-1})^c$	$(m^2 g^{-1})$	$(10^{-20} \text{ m}^2 \text{ V}^{-1})^c$
MoVTeNbO	1.1	0.8	15.5	2.5	13.6	2.2	9.8	1.6
H ₂ O ₂ treated MoVTeNbO	3.5	3.7	50.1	7.6	65.7	9.9	23.1	3.5
MoVO	2.9	6.0	40.5	2.5	105.3	6.4	20.8	1.3
MoVTeNbO-ht d	0.56		7.9	0.9			4.2	0.48

^a At 0.002 P/P₀

^b product of weight per V or Mo and the area in m² g⁻¹

^b Derived from measured metal composition and stoichiometries of MoO₃, VO_{2.5}, TeO₂, NbO_{2.5} for O atoms

^c Values reported in Ref. [23]

^b Area of a cylinder of 0.4 nm diameter with volume equal to the micropore volume

^c Product of weight per V or Mo in Table 2 and the area in m² g⁻¹

^d Values reported in Ref. [23]

Table 4. First-order C-H activation rate constant at different temperatures on VO_x/SiO₂, MoO₃, MoVTeNbO, H₂O₂ treated MoVTeNbO and MoVO.

Catalysts	Temperature (K)	$k_{ODH}K_{ads}^{a}$ (10 ⁻⁵ V ⁻¹ kPa ⁻¹ s ⁻¹)	Temperature (K)	$k_{ODH}K_{ads}^{b}$ (10 ⁻⁵ V ⁻¹ kPa ⁻¹ s ⁻¹)	
	C_2H_6ODH		C_6H_{12} ODH		
11% wt. VO_x/SiO_2	648	0.14	588	14.89	
	673	0.24	603	15.90	
	698	0.52	623	21.40	
	733	1.42	648	27.46	
			673	35.80	
MoO_3	673	0.003	603	0.172	
	698	0.006	623	0.282	
	733	0.020	648	0.498	
	773	0.050	673	0.840	
MoVTeNbO	648	2.43	603	3.14	
	673	4.14	623	4.78	
	698	7.28	648	8.67	
	733	16.06	673	14.59	
H ₂ O ₂ treated MoVTeNbO	648	13.21	603	26.08	
	673	22.71	623	41.11	
	698	36.56	648	77.17	
	733	71.96	673	102.29	
MoVO	648	44.44	603	27.94	
	673	82.98	623	49.46	
	698	126.96	648	76.72	
	733	261.56	673	119.86	

^a Derived from Equation 3 for measured rates at 3 kPa C₂H₆ and 0.5 kPa C₆H₁₂.

Table 5. Measured activation enthalpy and entropy values for C-H activation in C₂H₆ and C₆H₁₂ ODH on monometallic oxides and M1 phase mixed oxides. Uncertainties represent two times the standard errors.

Catalysts	$\Delta H_{C_2H_6}$	$\Delta H_{C_6H_{12}}$	$\Delta H_{C_2H_6}$ -	$\Delta S_{C_2H_6}$	$\Delta S_{C_6H_{12}}$	$\Delta S_{C_2H_6}$ -
	(kJ mol-	(kJ mol ⁻¹)	$\Delta H_{C_6H_{12}}$	(J ⁻¹ mol ⁻¹ K ⁻	(J-1 mol-1 K-	$\Delta S_{C_6H_{12}}$
	1)		(kJ mol ⁻¹)	1)	1)	(J ⁻¹ mol ⁻¹ K ⁻¹)
11% wt. VO _x /SiO ₂	105 (±15)	33 (±5)	+72 (±15)	-203 (±21)	-268 (±6)	+67 (±22)
41% wt. VO _x /SiO ₂ ^a	$78 (\pm 10)^a$	$40 \ (\pm 17)^a$	$+38 (\pm 17)^a$	-251 (±15) ^a	-263 (±28) a	+12 (±28) a
MoO_3	116 (±12)	71 (±1)	+45 (±12)	-223 (±17)	-243 (±1)	+20 (±17)
MoVTeNbO	82 (±6)	70 (±4)	$+13 (\pm 7)$	-213 (±3)	-222 (±6)	$+9 (\pm 11)$
H ₂ O ₂ treated MoVTeNbO	73 (±2)	63 (±13)	+10 (±13)	-213 (±9)	-215 (±20)	+2 (±20)
MoVO	75 (±6)	64 (±9)	$+12 (\pm 11)$	-199 (±9)	$-213(\pm 14)$	$+14 (\pm 17)$
MoVTeNbO-hta	79 (±5)	76 (±9)	$+3 (\pm 9)$	$-213 (\pm 7)$	$-215 (\pm 14)$	$+2 (\pm 14)$

^a Values reported in Ref. [23].

References

- [1] The Changing landscape of hydrocarbon feedstocks for chemical production; Alper, J., Ed.; National Academies Press: Washington, DC, Alper, J., Ed.; National Academies Press: Washington, DC2016.
- [2] F. Cavani, N. Ballarini, A. Cericola, Oxidative dehydrogenation of ethane and propane: How far from commercial implementation?, Catal. Today, 127 (2007) 113-131.
- [3] C.A. Gärtner, A.C. van Veen, J.A. Lercher, Oxidative dehydrogenation of ethane: common principles and mechanistic aspects, ChemCatChem, 5 (2013) 3196-3217.
- [4] M.D. Argyle, K. Chen, A.T. Bell, E. Iglesia, Ethane oxidative dehydrogenation pathways on vanadium oxide catalysts, J. Phys. Chem. B, 106 (2002) 5421-5427.
- [5] L. Annamalai, Y. Liu, P. Deshlahra, Selective C-H bond activation via NO_x mediated generation of strong H-abstractors, ACS Catal., 9 (2019) 10324-10338.
- [6] J.L. Nieto, P. Botella, M. Vázquez, A. Dejoz, The selective oxidative dehydrogenation of ethane over hydrothermally synthesised MoVTeNb catalysts, Chem. Commun., (2002) 1906-1907.
- [7] P. Botella, E. Garcia-González, A. Dejoz, J.L. Nieto, M. Vázquez, J. González-Calbet, Selective oxidative dehydrogenation of ethane on MoVTeNbO mixed metal oxide catalysts, J. Catal., 225 (2004) 428-438.
- [8] D. Melzer, G. Mestl, K. Wanninger, Y. Zhu, N.D. Browning, M. Sanchez-Sanchez, J.A. Lercher, Design and synthesis of highly active MoVTeNb-oxides for ethane oxidative dehydrogenation, Nat. Commun., 10 (2019) 1-9.
- [9] L. Espinal, K.A. Malinger, A.E. Espinal, A.M. Gaffney, S.L. Suib, Preparation of multicomponent metal oxides using nozzle spray and microwaves, Adv. Funct. Mater., 17 (2007) 2572-2579.
- [10] X. Chen, Q. Yang, B. Chu, H. An, Y. Cheng, Valence variation of phase-pure M1 MoVNbTe oxide by plasma treatment for improved catalytic performance in oxidative dehydrogenation of ethane, RSC Adv., 5 (2015) 91295-91301.
- [11] C. Baroi, A.M. Gaffney, R. Fushimi, Process economics and safety considerations for the oxidative dehydrogenation of ethane using the M1 catalyst, Catal. Today, (2017).

- [12] S. Ishikawa, W. Ueda, Microporous crystalline Mo-V mixed oxides for selective oxidations, Catal. Sci. Technol., 6 (2016) 617-629.
- [13] A. Trunschke, J. Noack, S. Trojanov, F. Girgsdies, T. Lunkenbein, V. Pfeifer, M. Hävecker, P. Kube, C. Sprung, F. Rosowski, The impact of the bulk structure on surface dynamics of complex Mo-V-based oxide catalysts, ACS Catal., 7 (2017) 3061-3071.
- [14] C.-c. Chiu, T. Vogt, L. Zhao, A. Genest, N. Rösch, Structure and electronic properties of MoVO type mixed-metal oxides—a combined view by experiment and theory, Dalton Trans., 44 (2015) 13778-13795.
- [15] P. DeSanto, D.J. Buttrey, R.K. Grasselli, C.G. Lugmair, A.F. Volpe, B.H. Toby, T. Vogt, Structural characterization of the orthorhombic phase M1 in MoVNbTeO propane ammoxidation catalyst, Top. Catal., 23 (2003) 23-38.
- [16] P. DeSanto, D.J. Buttrey, R.K. Grasselli, C.G. Lugmair, A.F. Volpe, B.H. Toby, T. Vogt, Structural aspects of the M1 and M2 phases in MoVNbTeO propane ammoxidation catalysts, Z. Krist., 219 (2004) 152-165.
- [17] W.D. Pyrz, D.A. Blom, T. Vogt, D.J. Buttrey, Direct Imaging of the MoVTeNbO M1 Phase Using An Aberration-Corrected High-Resolution Scanning Transmission Electron Microscope, Angew. Chem. Int. Ed., 47 (2008) 2788-2791.
- [18] W. Ueda, D. Vitry, T. Katou, Crystalline MoVO based complex oxides as selective oxidation catalysts of propane, Catal. Today, 99 (2005) 43-49.
- [19] N.R. Shiju, X. Liang, A.W. Weimer, C. Liang, S. Dai, V.V. Guliants, The role of surface basal planes of layered mixed metal oxides in selective transformation of lower alkanes: Propane ammoxidation over surface ab planes of Mo-V-Te-Nb-O M1 phase, J. Am. Chem. Soc., 130 (2008) 5850-5851.
- [20] D. Melzer, P. Xu, D. Hartmann, Y. Zhu, N.D. Browning, M. Sanchez-Sanchez, J.A. Lercher, Atomic-scale determination of active facets on the MoVTeNb oxide M1 phase and their intrinsic catalytic activity for ethane oxidative dehydrogenation, Angew. Chem. Int. Ed., 55 (2016) 8873-8877.
- [21] S. Ishikawa, X. Yi, T. Murayama, W. Ueda, Heptagonal channel micropore of orthorhombic Mo₃VO_x as catalysis field for the selective oxidation of ethane, Appl. Catal., A, 474 (2014) 10-17.

- [22] S. Ishikawa, X. Yi, T. Murayama, W. Ueda, Catalysis field in orthorhombic Mo₃VO_x oxide catalyst for the selective oxidation of ethane, propane and acrolein, Catal. Today, 238 (2014) 35-40.
- [23] L. Annamalai, Y. Liu, S. Ezenwa, Y. Dang, S.L. Suib, P. Deshlahra, Influence of tight confinement on selective oxidative dehydrogenation of ethane on MoVTeNb mixed oxides, ACS Catal., 8 (2018) 7051-7067.
- [24] Y. Liu, L. Annamalai, P. Deshlahra, Effects of lattice O atom coordination and pore confinement on selectivity limitations for ethane oxidative dehydrogenation catalyzed by vanadium-oxo species, J. Phys. Chem. C, 123 (2019) 28168-28191.
- [25] W. Ruettinger, A. Benderly, S. Han, X. Shen, Y. Ding, S.L. Suib, Influence of Support Surface Area and Niobium Addition on the Reactivity of Vanadium Catalysts for Propane Oxidative Dehydrogenation, Catal. Lett., 141 (2011) 15-21.
- [26] A.C. Sanfiz, T.W. Hansen, F. Girgsdies, O. Timpe, E. Rödel, T. Ressler, A. Trunschke, R. Schlögl, Preparation of phase-pure M1 MoVTeNb oxide catalysts by hydrothermal synthesis-influence of reaction parameters on structure and morphology, Top. Catal., 50 (2008) 19-32.
- [27] T. Nguyen, M. Aouine, J. Millet, Optimizing the efficiency of MoVTeNbO catalysts for ethane oxidative dehydrogenation to ethylene, Catal. Commun., 21 (2012) 22-26.
- [28] T. Konya, T. Katou, T. Murayama, S. Ishikawa, M. Sadakane, D. Buttrey, W. Ueda, An crthorhombic Mo₃VO_x catalyst most active for oxidative dehydrogenation of ethane among related complex metal oxides, Catal. Sci. Technol., 3 (2013) 380-387.
- [29] S. Barman, N. Maity, K. Bhatte, S. Ould-Chikh, O. Dachwald, C. Haeßner, Y. Saih, E. Abou-Hamad, I. Llorens, J.-L. Hazemann, Single-site VO_x moieties generated on silica by surface organometallic chemistry: a way to enhance the catalytic activity in the oxidative dehydrogenation of propane, ACS Catal., 6 (2016) 5908-5921.
- [30] A. Khodakov, J. Yang, S. Su, E. Iglesia, A.T. Bell, Structure and properties of vanadium oxide-zirconia catalysts for propane oxidative dehydrogenation, J. Catal., 177 (1998) 343-351.
- [31] B. Chu, L. Truter, T.A. Nijhuis, Y. Cheng, Oxidative dehydrogenation of ethane to ethylene over phase-pure M1 MoVNbTeO_x catalysts in a micro-channel reactor, Catal. Sci. Technol., 5 (2015) 2807-2813.

- [32] B. Chu, L. Truter, T. Nijhuis, Y. Cheng, Performance of phase-pure M1 MoVNbTeOx catalysts by hydrothermal synthesis with different post-treatments for the oxidative dehydrogenation of ethane, Appl. Catal., A, 498 (2015) 99-106.
- [33] M.D. Argyle, K. Chen, A.T. Bell, E. Iglesia, Effect of catalyst structure on oxidative dehydrogenation of ethane and propane on alumina-supported vanadia, J. Catal., 208 (2002) 139-149.
- [34] C.A. Carrero, C.J. Keturakis, A. Orrego, R. Schomäcker, I.E. Wachs, Anomalous reactivity of supported V₂O₅ nanoparticles for propane oxidative dehydrogenation: influence of the vanadium oxide precursor, Dalton Trans., 42 (2013) 12644-12653.
- [35] C.A. Carrero, R. Schloegl, I.E. Wachs, R. Schomaecker, Critical literature review of the kinetics for the oxidative dehydrogenation of propane over well-defined supported vanadium oxide catalysts, ACS Catal., 4 (2014) 3357-3380.
- [36] A. Pan, J.-G. Zhang, Z. Nie, G. Cao, B.W. Arey, G. Li, S.-q. Liang, J. Liu, Facile synthesized nanorod structured vanadium pentoxide for high-rate lithium batteries, J. Mater. Chem., 20 (2010) 9193-9199.
- [37] H. Hu, C. Deng, J. Xu, K. Zhang, M. Sun, Metastable h-MoO₃ and stable α-MoO₃ microstructures: controllable synthesis, growth mechanism and their enhanced photocatalytic activity, J. Exp. Nanosci., 10 (2015) 1336-1346.
- [38] Y.V. Kolen'ko, W. Zhang, R.N. d'Alnoncourt, F. Girgsdies, T.W. Hansen, T. Wolfram, R. Schloegl, A. Trunschke, Synthesis of MoVTeNb oxide catalysts with tunable particle dimensions, ChemCatChem, 3 (2011) 1597-1606.
- [39] Q. He, J. Woo, A. Belianinov, V.V. Guliants, A.Y. Borisevich, Better catalysts through microscopy: mesoscale M1/M2 intergrowth in Molybdenum–Vanadium based complex oxide catalysts for propane ammoxidation, ACS Nano, 9 (2015) 3470-3478.
- [40] M. Sadakane, K. Kodato, T. Kuranishi, Y. Nodasaka, K. Sugawara, N. Sakaguchi, T. Nagai, Y. Matsui, W. Ueda, Molybdenum-vanadium-based molecular sieves with microchannels of seven-membered rings of corner-sharing metal oxide octahedra, Angew. Chem. Int. Ed., 47 (2008) 2493-2496.

- [41] B. Deniau, G. Bergeret, B. Jouguet, J. Dubois, J. Millet, Preparation of single M1 phase MoVTe (Sb) NbO catalyst: Study of the effect of M2 phase dissolution on the structure and catalytic properties, Top. Catal., 50 (2008) 33-42.
- [42] T.Y. Kardash, L.M. Plyasova, V.M. Bondareva, T.V. Andrushkevich, L.S. Dovlitova, A.I. Ischenko, A.I. Nizovskii, A.V. Kalinkin, M₅O₁₄-like V-Mo-Nb oxide catalysts: structure and catalytic performance, Appl. Catal., A, 375 (2010) 26-36.
- [43] J. Woo, U. Sanghavi, A. Vonderheide, V.V. Guliants, A study of M1/M2 phase synergy in the MoVTe(Nb,Ta) O catalysts for propane ammoxidation to acrylonitrile, Appl. Catal., A, 515 (2016) 179-189.
- [44] D. Vitry, Y. Morikawa, J. Dubois, W. Ueda, Mo-V-Te-(Nb)-O mixed metal oxides prepared by hydrothermal synthesis for catalytic selective oxidations of propane and propene to acrylic acid, Appl. Catal., A, 251 (2003) 411-424.
- [45] T. Vogt, D. Blom, L. Jones, D. Buttrey, ADF-STEM imaging of nascent phases and extended disorder within the Mo-V-Nb-Te-O catalyst system, Top. Catal., 59 (2016) 1489-1495.
- [46] M. Aouine, T. Epicier, J.-M.M. Millet, In situ environmental STEM study of the MoVTe oxide M1 phase catalysts for ethane oxidative dehydrogenation, ACS Catal., 6 (2016) 4775-4781.
- [47] M. Sadakane, K. Yamagata, K. Kodato, K. Endo, K. Toriumi, Y. Ozawa, T. Ozeki, T. Nagai, Y. Matsui, N. Sakaguchi, Synthesis of orthorhombic Mo-V-Sb oxide species by assembly of pentagonal Mo₆O₂₁ polyoxometalate building blocks, Angew. Chem. Int. Ed., 48 (2009) 3782-3786.
- [48] S. Brunauer, P.H. Emmett, E. Teller, Adsorption of Gases in Multimolecular Layers, Journal of the American Chemical Society, 60 (1938) 309-319.
- [49] S. Ishikawa, Y. Yamada, C. Qiu, Y. Kawahara, N. Hiyoshi, A. Yoshida, W. Ueda, Synthesis of a crystalline orthorhombic Mo-V-Cu oxide for selective oxidation of acrolein, Chem. Mater., 31 (2019) 1408-1417.
- [50] J. García-Martínez, D. Cazorla-Amorós, A. Linares-Solano, Further evidences of the usefulness of CO₂ adsorption to characterize microporous solids, in: K.K. Unger, G. Kreysa, J.P. Baselt (Eds.) Stud. Surf. Sci. Catal., Elsevier2000, pp. 485-494.

- [51] J. Luo, Q. Zhang, J. Garcia-Martinez, S.L. Suib, Adsorptive and acidic properties, reversible lattice oxygen evolution, and catalytic mechanism of cryptomelane-type manganese oxides as oxidation catalysts, J. Am. Chem. Soc., 130 (2008) 3198-3207.
- [52] M. Zboray, A.T. Bell, E. Iglesia, Role of C-H bond strength in the rate and selectivity of oxidative dehydrogenation of alkanes, J. Phys. Chem. C, 113 (2009) 12380-12386.
- [53] K. Chen, A.T. Bell, E. Iglesia, Kinetics and mechanism of oxidative dehydrogenation of propane on vanadium, molybdenum, and tungsten oxides, J. Phys. Chem. B, 104 (2000) 1292-1299.
- [54] J.A. Muller, W.C. Conner, Cyclohexane in ZSM 5. 1. FTIR and x-ray studies, J. Phys. Chem., 97 (1993) 1451-1454.
- [55] T.W. Birky, J.T. Kozlowski, R.J. Davis, Isotopic transient analysis of the ethanol coupling reaction over magnesia, J. Catal., 298 (2013) 130-137.
- [56] H. Eyring, The activated complex in chemical reactions, J. Chem. Phys., 3 (1935) 107-115.
- [57] A. Klisińska, K. Samson, I. Gressel, B. Grzybowska, Effect of additives on properties of V₂O₅/SiO₂ and V₂O₅/MgO catalysts: I. Oxidative dehydrogenation of propane and ethane, Appl. Catal., A, 309 (2006) 10-16.
- [58] Y. Zhu, P.V. Sushko, D. Melzer, E. Jensen, L. Kovarik, C. Ophus, M. Sanchez-Sanchez, J.A. Lercher, N.D. Browning, Formation of oxygen radical sites on MoVNbTeO_x by cooperative electron redistribution, J. Am. Chem. Soc., 139 (2017) 12342-12345.